

Gaia DR2 giants in the Galactic dust – I. Reddening across the whole dust layer and some properties of the giant clump.

George A. Gontcharov,^{1,2*} and Aleksandr V. Mosenkov³

¹Department for Management of Science and Technology Development, Ton Duc Thang University, Ho Chi Minh City, Vietnam

²Faculty of Applied Sciences, Ton Duc Thang University, Ho Chi Minh City, Vietnam

³Central Astronomical Observatory, Russian Academy of Sciences, 65/1 Pulkovskoye chaussee, St. Petersburg, 196140 Russia

Accepted 2020 September 07. Received 2020 September 03; in original form 2020 April 15

ABSTRACT

We consider a complete sample of 101 810 giants with *Gaia* Data Release 2 (DR2) parallaxes ϖ within the red clump domain of the Hertzsprung–Russell diagram in the space cylinder with a radius of 700 pc around the Sun and a height of $|Z| = 1800$ pc. We use the *Gaia* DR2 G_{BP} , G_{RP} and *Wide-field Infrared Survey Explorer* (*WISE*) $W3$ photometry. We describe the spatial variations of the modes of the observables $G_{BP} - G_{RP}$, $G_{RP} - W3$, $G_{BP} + 5 + 5 \log_{10} \varpi$, $G_{RP} + 5 + 5 \log_{10} \varpi$, and $W3 + 5 + 5 \log_{10} \varpi$ by extinction and reddening in combination with linear vertical gradients of the intrinsic colours and absolute magnitudes of the red giant clump. The derived clump median absolute magnitude in $W3$ agrees with its recent literature estimates. The clump median intrinsic colours and absolute magnitudes in G_{BP} and G_{RP} are derived for the first time at a precision level of 0.01 mag. We confirm the reliability of the derived clump absolute magnitudes, intrinsic colours, and their vertical gradients by comparing them with the theoretical predictions from the PADova and TRIeste Stellar Evolution Code, MESA Isochrones and Stellar Tracks and Bag of Stellar Tracks and Isochrones isochrones. This leads us to the median age and $[Fe/H]$ of the clump within $|Z| < 1.7$ kpc from the Galactic mid-plane as $(2.3 \pm 0.5) + (3.2 \pm 1.6) |Z|$ Gyr and $(-0.08 \pm 0.08) - (0.16 \pm 0.07) |Z|$ dex, respectively, where Z is expressed in kpc. These results agree with recent empirical and theoretical estimates. Moreover, all the models give similar age–metallicity relations by use of our results in the optical range. The derived extinctions and reddenings across the whole dust half-layer below or above the Sun converge to the reddening $E(B - V) = 0.06$ mag by use of the most reliable extinction laws.

Key words: dust, extinction – stars: late-type – ISM: structure – local interstellar matter – solar neighbourhood

1 INTRODUCTION

The properties of the Galactic dust layer typically have been derived from photometry and other data of stars embedded into or seen through this layer. However, inaccurate distances and photometry cause these properties to still be scarcely understood.

The best data available before the *Gaia* mission (*Gaia* Collaboration 2018a,b), such as the *Hipparcos* parallaxes (van Leeuwen 2007), cover only a hundred parsecs from the Sun. Therefore, they provide no precise data for determining (i) the dust layer scale height, (ii) related extinction through the whole dust half-layer below or above the Sun and, consequently, (iii) extinction to high-latitude objects situated behind the layer.

As a result, various estimates of these quantities appear to be contradictory. For example, Gontcharov & Mosenkov (2018) recently revised the reddening across the whole dust layer. We used data from the *Gaia* Data Release 1 (DR1) Tycho–*Gaia* Astrometric Solution (TGAS; Michalik, Lindegren & Hobbs 2015) for giants within 415 pc from the Sun, in combination with their extinction/reddening es-

timates from various maps and models¹. We compared the position of these giants in the Hertzsprung–Russell (HR) diagrams among the isochrones from PADova and TRIeste Stellar Evolution Code (PARSEC; Marigo et al. 2017²) and MESA Isochrones and Stellar Tracks (MIST; Paxton et al. 2011, 2013; Choi et al. 2016; Dotter 2016³). The TRILEGAL Galaxy model (Girardi et al. 2005) with its parameters widely varied was also used. We found that, given a reliable solar metallicity, the median reddening at Galactic latitudes $|b| > 50^\circ$, far from the Galactic mid-plane, is $E(B - V) > 0.04$ mag, with its most probable estimate $E(B - V) = 0.06$ mag. This evidence agrees with the estimates of Teerikorpi (1990), Gontcharov (2017a, hereafter G17), and Gontcharov & Mosenkov (2019). However, this contrasts with the estimates within $0.01 < E(B - V) < 0.02$ mag from the widely used 2D reddening maps of Schlegel, Finkbeiner & Davis (1998, hereafter SFD98) and Meisner & Finkbeiner (2015, hereafter MF15) and 3D reddening maps of Drimmel, Cabrera-Lavers & López-Corredoira (2003, hereafter DCL03) and Lallement et al. (2019, hereafter LVV19). Thus,

¹ A map is a representation in a tabular view, while a model is a representation given by some formulas.

² <http://stev.oapd.inaf.it/cgi-bin/cmd>

³ <http://waps.cfa.harvard.edu/MIST/>

* E-mail: george.gontcharov@tdtu.edu.vn

the reddening across the whole dust layer needs to be further explored.

Besides that, different authors provide different estimates of the dust layer scale height (Perryman 2009, pp. 469–472). For example, they include: 35 – 55 (Vergely et al. 1998), < 70 (Jurić et al. 2008), ≈ 100 (Gontcharov 2012b, hereafter G12), 140 (Robin et al. 2003), and 188 pc (Drimmel & Spergel 2001).

The dust that provides a considerable reddening exists much behind the scale height of the dust layer. For example, 5 per cent of dust (and corresponding reddening) is behind the three scale heights if the dust vertical distribution is described by an exponential law: $\sim e^{-|Z-Z_0|/Z_A}$ (Parenago 1954, p. 265), where Z is the Galactic rectangular coordinate directed to the North Galactic pole, Z_A is the scale height of the dust layer and Z_0 is the vertical offset of the dust layer mid-plane w.r.t. the Sun. Hence, to take into account more than 95 per cent of the reddening across the whole dust layer, we have to consider stars within, at least, $3Z_A$, i.e. $|Z| < 188 \times 3 = 564$ pc. Consequently, the distances to them need to be accurately estimated.

Moreover, there may exist a degeneracy between the reddening and the vertical (i.e. along $|Z|$) gradient of a star intrinsic (dereddened) colour, as well as between the extinction and the vertical gradient of a star absolute magnitude. To avoid this degeneracy, we should consider a wide range of $|Z|$ in a space beyond the Galactic dust layer, i.e., at least, for $500 < |Z| < 1000$ pc. In this space, the gradients are high, but the variations of the reddening and extinction are minimal.

At such high $|Z|$, *Gaia* DR2 is the first all-sky source of accurate parallaxes. It allows us to consider a complete sample of rather luminous stars from *Gaia* DR2 in such a space. It must be a common type of stars with accurate photometry in the whole space under consideration. These stars must be easily selected in the HR diagram using their photometry and parallaxes. Therefore, we consider the red giant clump domain in the HR diagram.

This domain contains a mix of giants of the clump, branch, and asymptotic branch. They differ by the nuclear fusion inside them: core helium for the clump, envelope hydrogen for the branch, and both constituents for the asymptotic branch. Among them, the red clump giants are suitable for our study, being ‘standard candles’ with rather small and predictable variations of their intrinsic colours and absolute magnitudes (Girardi 2016). However, empirical estimates of the clump intrinsic colours and absolute magnitudes contradict each other (Ruiz-Dern et al. 2018, hereafter RBA18). Moreover, they show a large discrepancy with their theoretical predictions (Girardi 2016). Thus, the clump intrinsic characteristics need further investigation.

Gontcharov (2008, 2009) has shown that a sample of all stars in the clump domain, selected by use of accurate data, contains a majority of red clump giants and a minority of branch and asymptotic branch giants. Then a pure sample of red clump giants can be created by removing branch and asymptotic branch contaminants, if one uses some assumptions and/or additional photometric, spectroscopic or asteroseismic data (see, e.g. Gontcharov 2009; Chen et al. 2017).

However, in this study we use another approach thanks to high *Gaia* DR2 precision. Instead of cleaning the sample of all stars in the clump domain, we consider modes of their observables. To obtain the modes, we round the observables up to 0.01 mag and find the tops of their histograms in each spatial cell. In the case of multimodal histograms, the lowest value is selected, since it is more probable for the unreddened or slightly reddened clump. In this approach, we follow Gontcharov (2017b). He has shown that the modes of colours, dereddened colours, magnitudes and absolute magnitudes for such a sample are completely defined by red clump giants. In contrast, their mean and median vary considerably due to the influence of branch and asymptotic branch giants.

The aim of this paper is to derive with minimal assumptions (i) reddening and extinction estimates across the whole Galactic dust layer by use of the red clump giants as extinction probes, (ii) dereddened colours and absolute magnitudes of the red giant clump, and (iii) some vertical gradients of these quantities due to vertical gradients of age and metallicity of the clump.

This paper is organized as follows. In Sect. 2 we select a sample of *Gaia* DR2 giants. In Sect. 3 we analyse the spatial variations of the modes of some observables in order to estimate the extinction and reddening along the Galactic mid-plane and across the dust layer, as well as the intrinsic colours and absolute magnitudes of the red clump giants. We compare them with both empirical and theoretical estimates and derive an age–metallicity relation (AMR) in Sect. 4. We discuss different estimates of the reddening across the whole dust layer in Sect. 5. We summarize our findings and state our conclusions in Sect. 6.

2 DATA

To study the properties of the red clump giants in the Galactic dust, we consider a properly constrained space. The space under consideration is limited by: (i) the precision of the *Gaia* DR2 parallaxes, which should be better than 10 per cent, (ii) the predictability of the properties of the dust layer and the stars embedded within it, despite their variations along the X , Y and Z Galactic coordinates (see, e.g. Drimmel & Spergel 2001), (iii) the need for a wide range of Z . Therefore, we consider a space cylinder with a radius of 700 pc around the Sun, elongated up to $|Z| < 1800$ pc along the Z -axis.

This space is especially appropriate to avoid the degeneracy between the reddening and intrinsic gradients. The reddening is determined more accurately in regions far from the Sun, near the Galactic mid-plane, while the gradients are determined more accurately in regions above or below the Sun, far from the mid-plane.

To derive robust properties of the dust layer, we need a rather long wavelength baseline, i.e. with optical and infrared (IR) bands. Gontcharov (2016a, table 1) has estimated the distance ranges where a sample of red clump giants with an accurate photometry in various bands is complete. In the space cylinder under consideration, the *Wide-field Infrared Survey Explorer* (*WISE*, allWISE, Wright et al. 2010) $W3$ photometry at 10.8 microns provides the most complete sample of the red giant clump among all bands of IR all-sky surveys. Its photometric precision is < 0.06 mag for all stars, with a median precision of 0.017 mag. By use of the Two Micron All-Sky Survey (2MASS, Skrutskie et al. 2006) J , H , K_s and *WISE* $W1$, $W2$, $W4$ photometry of the same precision, we would lose about 2, 10, 2, 43, 8 and 82 per cent of the stars with the $W3$ photometry, respectively. Moreover, the saturation of all nearby giants in the J , H , K_s , $W1$ and $W2$ bands would lead to undesirable removal of giants with a little or zero reddening.

Finally, we use the G_{BP} and G_{RP} bands from *Gaia* DR2 in combination with the $W3$ band from *WISE*. We use the *WISE* versus *Gaia* DR2 cross-identification in order to select all stars in the clump domain of the HR diagram.

The domain must be constrained in order to keep the main concentration of the giants, i.e. their clump, well inside this domain, whether the extinction and reddening are taken into account or not. In such a case, no correction for reddening and extinction has to be applied during the sample selection. To fulfill this, any variation of modes of the observables due to reasonable variations of age, metallicity, reddening and extinction law within the space under consideration should keep them within the selection domain. To constrain the domain, we

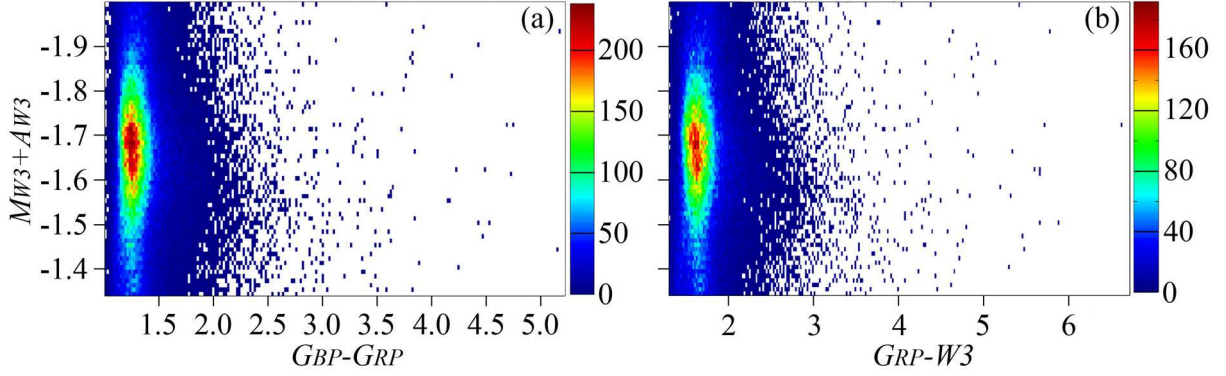


Figure 1. The initial HR diagrams (a) ‘ $G_{BP} - G_{RP}$ versus $M_{W3} + A_{W3}$ ’ and (b) ‘ $G_{RP} - W3$ versus $M_{W3} + A_{W3}$ ’ for the selected sample. The bins are 0.02 and 0.01 mag for the abscissas and ordinates, respectively. The number of stars in each bin is shown by the colour scale on the right.

use reliable data sources, such as TRILEGAL, 3D reddening map of DCL03⁴, and extinction law of Wang & Chen (2019, hereafter WC19)⁵. The domain is constrained as:

$$G_{BP} - G_{RP} > 1, \quad (1)$$

$$G_{RP} - W3 > 1.3, \quad (2)$$

$$-2 < W3 + 5 + 5 \log_{10} \varpi < -1.35, \quad (3)$$

where ϖ is the parallax from *Gaia* DR2. Hereafter, we also use the distances R derived from ϖ by Bailer-Jones et al. (2018). Equation (3) is equivalent to

$$-2 < M_{W3} + A_{W3} < -1.35, \quad (4)$$

taking into account

$$W3 + 5 + 5 \log_{10} \varpi = M_{W3} + A_{W3}, \quad (5)$$

where M_{W3} and A_{W3} are absolute magnitude and extinction in $W3$, respectively. Similarly to observable (5), we can consider the observables

$$G_{BP} + 5 + 5 \log_{10} \varpi = M_{G_{BP}} + A_{G_{BP}}, \quad (6)$$

$$G_{RP} + 5 + 5 \log_{10} \varpi = M_{G_{RP}} + A_{G_{RP}}. \quad (7)$$

We remove stars with a negative parallax or with the fractional parallax uncertainty (the ratio of the parallax uncertainty to the parallax) higher than 0.354, since they have no precise distance (Bailer-Jones 2015).

Since the modes of observables (1), (2), (5), (6) and (7) are always inside the selection domain, the following relations are true for the red giant clump:

$$\text{mode}(M_{G_{BP}} + A_{G_{BP}}) = \text{mode}(M_{G_{BP}}) + A_{G_{BP}}, \quad (8)$$

$$\text{mode}(M_{G_{RP}} + A_{G_{RP}}) = \text{mode}(M_{G_{RP}}) + A_{G_{RP}}, \quad (9)$$

$$\text{mode}(M_{W3} + A_{W3}) = \text{mode}(M_{W3}) + A_{W3}, \quad (10)$$

$$\text{mode}(G_{BP} - G_{RP}) = \text{mode}((G_{BP} - G_{RP})_0) + E(G_{BP} - G_{RP}), \quad (11)$$

$$\text{mode}(G_{RP} - W3) = \text{mode}((G_{RP} - W3)_0) + E(G_{RP} - W3), \quad (12)$$

We remove 98 stars with the *Gaia* DR2 `phot_bp_rp_excess_factor` $\equiv (F_{BP} + F_{RP})/F_G > 1.3 + 0.06(G_{BP} - G_{RP})^2$, where F_{BP} , F_{RP} , and F_G are the fluxes within the *Gaia* filters. The reason of their removal is that they are not ‘well-behaved single sources’ (Gaia Collaboration 2018b).

172 stars appear outliers in the diagram $G_{BP} - G_{RP}$ versus $G_{RP} - W3$, apparently, due to a wrong *Gaia* DR2 – *WISE* cross-identification. We remove these outliers by use of our empirical relation for the remaining stars: $G_{RP} - W3 < 0.86 + 1.3(G_{BP} - G_{RP})$.

The spatial distribution of the rejected stars is quite uniform, therefore their removal does not influence our results.

The final sample contains 101 810 giants. In Table 1 we list some important information on the selected sample. The median relative error of R in the sample is 2 per cent. Only 720 stars (0.7 per cent) have a relative error of R larger than 10 per cent. The photometry of the selected stars is very precise: $\sigma(G_{BP}) < 0.05$ and $\sigma(G_{RP}) < 0.03$ mag for all the stars, while the medians are $\sigma(G_{BP}) = \sigma(G_{RP}) = 0.001$ mag.

The distribution of the sample inside the selection domain in the HR diagrams is shown in Fig. 1.

The completeness of the sample is evident from Fig. 2 where the sample is projected into the XY plane in the bins of 20×20 pc. It shows no artifact and no decrease to the periphery, but only an expected gradient to the Galactic Centre (to the right).

The distribution of the sample by Z is shown in Fig. 3. This can be compared with figure 6 of Gontcharov (2008). The most reliable exponential approximation of this distribution, with a scale height of 325 pc and a maximum spatial density at 20 pc south from the Sun, is shown in Fig. 3 by the red line. Accordingly, both the mean and median values of Z in the sample is -22 pc. This deviation from zero reflects the shift of the Galactic mid-plane from the Sun. The scale height and the offset of the Sun differ from the previous estimates

⁴ The DCL03 estimates are calculated by use of the code of Bovy et al. (2016), <https://github.com/jobovy/mwdust>

⁵ Hereafter, using the law of WC19, we take into account the dependencies of the extinction coefficients on the spectral energy distribution and the extinction itself by use of the curves from figure 2 of WC19. However, as seen from that figure, for the vast majority of our stars this changes $A_{G_{BP}}$ and $A_{G_{RP}}$ by only a few per cent, while A_{W3} does not change at all. Therefore, our results and conclusions are not affected by these dependencies.

Table 1. The main data for the selected sample: source_id, right ascension and declination for the epoch 2015.0 (deg), parallax (mas), standard error of parallax (mas), Galactic longitude and latitude for the epoch 2015.0 (deg), distance r_{est} from [Bailer-Jones et al. \(2018\)](#) (parsec), G_{BP} (mag), G_{RP} (mag), and $W3$ from the allWISE catalogue (mag). All the data are from *Gaia* DR2, except r_{est} and $W3$. The complete table is available online.

Source_id	RA	DEC	ϖ	e_{ϖ}	l	b	r_{est}	G_{BP}	G_{RP}	$W3$
1000049810224526080	104.450301	55.980873	2.83	0.04	160.365533	23.064404	350.18	9.453	8.071	6.290
100013467877721088	103.017215	55.776143	3.60	0.05	160.348636	22.235018	275.68	8.668	7.323	5.570
1000344651138651776	102.573738	56.874385	2.85	0.11	159.134517	22.299573	347.67	8.686	7.439	5.817
1000594171558726656	104.647456	57.390965	1.28	0.05	158.907905	23.520080	762.58	10.347	9.293	7.956
1000598668388532864	104.438721	57.496416	1.28	0.04	158.766577	23.436812	762.24	10.615	9.314	7.615
...

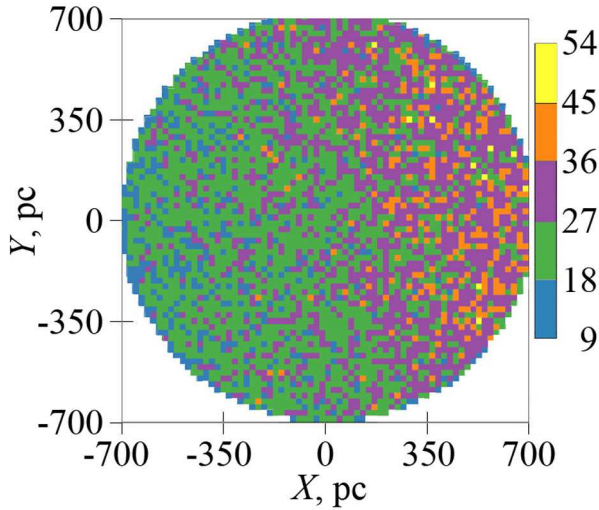


Figure 2. The sample projected into the XY plane in the bins of 20×20 pc. The number of stars in each bin is shown by the colour scale on the right. The Sun is at the centre. The Galactic Centre is to the right.

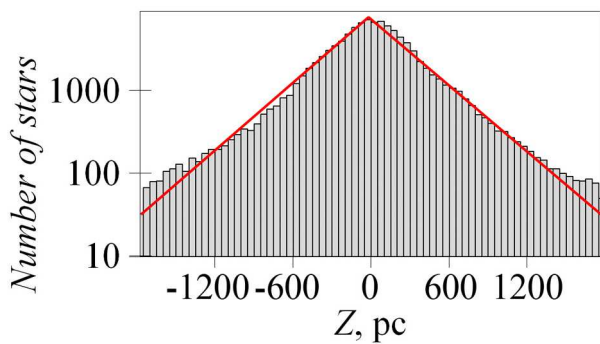


Figure 3. The distribution of the sample by Z . The most reliable exponential approximation of this distribution with a scale height of 325 pc is shown by the red line.

obtained by [Gontcharov \(2008\)](#), 280 and 13 pc, respectively, due to a higher completeness of the current sample. The median $|Z|$ of the sample is 212 pc. 73 and 90 per cent of the sample are within $|Z| < 400$ and < 700 pc, respectively. Consequently, the majority of stars seem to be inside the dust layer.

To consider the spatial distribution of the sample in detail, one

has to separate the clump, branch and asymptotic branch giants from their mix. However, this is out of the scope of this paper.

3 SPATIAL VARIATIONS OF THE OBSERVABLES

The main assumptions of our approach are defined by equations (8)–(12). Apart from those, we use the following:

(i) Any spatial variations of the dereddened colours and absolute magnitudes of the clump can be presented as their linear vertical and radial gradients. The former is a gradient along $|Z|$, while the latter is a gradient along the galactocentric position. This position, w.r.t. the solar circle, is calculated as $X' = R_{\odot} - ((R_{\odot} - X)^2 + Y^2 + Z^2)^{0.5}$, where $R_{\odot} = 8200$ pc is the adopted distance from the Sun to the Galactic Centre ([Perryman 2009](#), pp. 495–496). We define X' to be positive towards the Galactic Centre. Our space cylinder covers the range $-868 < X' < 699$ pc. The uncertainty of R_{\odot} has a negligible effect on our results, since we consider a Galactic vicinity of the Sun. For the same reason, X' is close to X .

(ii) The dust volume density has a very shallow gradient with $|Z|$ in regions far from the Galactic mid-plane. More precisely, cumulative extinction and reddening have a negligible increase with $|Z|$ at $|Z| > 400$ pc.

To analyse the spatial variations of observables (8)–(12), we need to calculate their modes in some small spatial cells. As mentioned in Sect. 1, to obtain the modes, we round the observables up to 0.01 mag and find the tops of their histograms in each cell. An example of the histograms for a cell with a rather high extinction and reddening is shown in Fig. 4. It shows long red tails of $G_{BP} - G_{RP}$ and $G_{RP} - W3$ due to reddening and, what is less important, due to the branch and asymptotic branch contaminants. The observed asymmetry of the $M_{W3} + A_{W3}$ histogram is caused by the contaminants. Despite this, the modes are determined fairly confidently.

Various uncertainties contribute to the total uncertainty of the modes. Three uncertainties seem to be most important: (i) the photometric uncertainty, (ii) the uncertainty due to random fluctuations of the stellar content in the cell with higher or lower percentage of the clump giants w.r.t. the contaminants, and (iii) the uncertainty due to natural fluctuations of the interstellar medium between us and the stars in the cell, followed by related fluctuations of the extinction, reddening and observables.

We expect that the uncertainties (i) and (ii) decrease with an increasing number of stars in a cell and, in turn, with an increasing size of the cell. In contrast, the uncertainty (iii) has a little, if any,

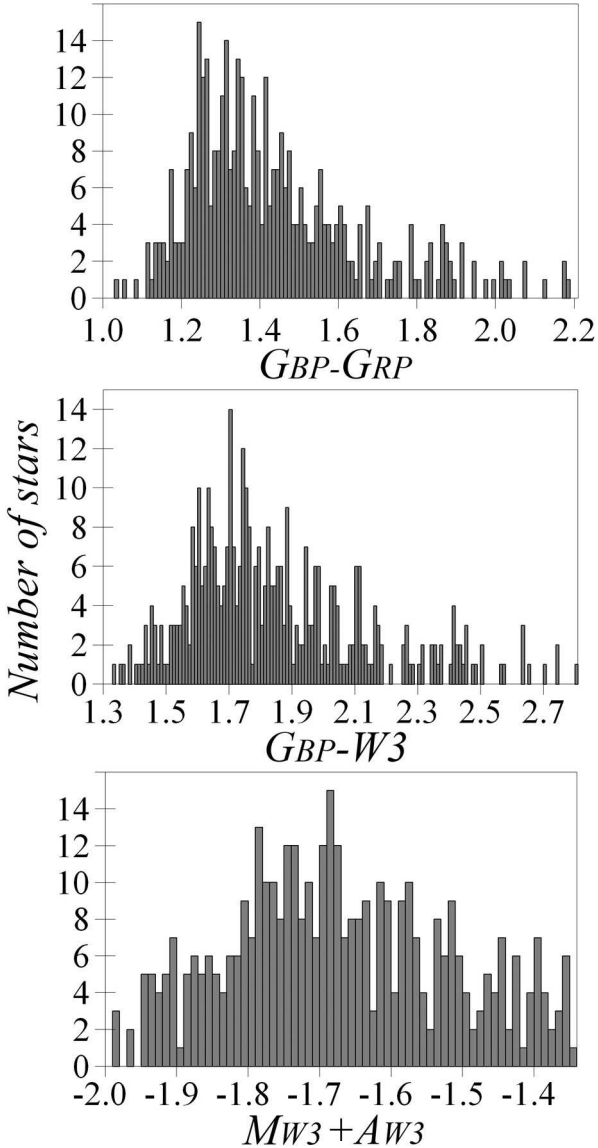


Figure 4. Histograms of some observables in a spatial cell with 400 giants from our sample.

decrease with an increasing size of the cell, since the medium fluctuations increase with the size (see, e.g. Gontcharov 2019). Hence, an optimal number of stars in a cell (and an optimal cell size) must exist. With this or greater number of stars in a cell, the uncertainty (iii) dominates in the total uncertainty. We select the optimal number of stars in a cell empirically: by increasing it until the standard deviation of the modes of the observables in adjacent spatial cells is stabilized. The optimal number appears to be 400 stars.

We can consider the standard deviation of the modes, since the fluctuations of the medium from cell to cell are random. Consequently, with the dominance of the uncertainty (iii), we expect to see a random scatter of the modes of the observables in several independent cells.

The formal precision of the derived modes is 0.01 mag. However, their accuracy is defined by the medium fluctuations. This accuracy varies from 0.01 mag for cells near the Sun and at high-latitudes up to several hundredths of a magnitude in distant cells near the Galactic mid-plane (Gontcharov 2019). Consequently, we expect the

uncertainty of an average or a gradient, derived from many cells, to be at a level of 0.01 mag.

A sample of unreddened giants is needed to derive their intrinsic characteristics and also as a reference for reddened giants. However, we cannot create such a sample from the nearest giants. Indeed, to select 400 nearest giants, we have to consider a vicinity of 111 pc around the Sun. However, Gontcharov & Mosenkov (2019) show that the extinction and reddening are the lowest, yet, not negligible at an accuracy level of 0.01 mag even in the Local Cavity, or Local Bubble, a region within about 80 pc from the Sun. Therefore, any extinction or reddening estimate in this space should be considered only as an upper limit of the estimate at $R = 0$. Moreover, due to the nearly uniform spatial distribution of the sample giants near the Galactic mid-plane, half of them, being within $R < 111$ pc have, in fact, $92 < R < 111$ pc. Naturally, they have a typical reddening of several hundredths of a magnitude. Considering such slightly reddened stars as unreddened ones, one would introduce a bias to any further estimate of the reddening for distant stars. This bias is especially important at high-latitudes where it is comparable to the observed low reddening and, therefore, makes it very uncertain.

3.1 The thin coordinate layer

We can estimate the dereddened colours and absolute magnitudes for nearby clump giants by extrapolating the moving modes of the observables to $R = 0$. The moving modes are calculated using a window of 400 stars. We consider a thin coordinate layer of $|Z| < 40$ pc with 10 802 stars.

The thickness of this coordinate layer is set in a way that it certainly contains a significant mass of dust. Also the coordinate layer must contain the mid-plane of the dust layer, despite the shift Z_0 of this mid-plane from the Sun. This shift is known worse than the shifts of the Sun from some stellar distribution mid-planes and from the geometrical Galactic mid-plane. However, this shift can be estimated as $10 < Z_0 < 30$ pc (see the discussion in Gontcharov 2012c). Therefore, the thickness of the thin coordinate layer as $|Z| < 40$ pc seems to be appropriate. Similarly, Vergely et al. (1998) have considered the reddening within a thin coordinate layer of $|Z| < 40$ pc in order to derive some properties of the dust medium near the Galactic mid-plane.

In total, we calculate $10\,802 - 400 = 10\,402$ moving modes. Only $10\,802/400 \approx 27$ of them are independent from each other. We apply a resampling method to check the robustness of our results⁶. Namely, we reproduce our results with many randomly selected subsamples of 27 modes out of 10 402. The results for these realizations of the resampling method appear the same as those for the 10 402 moving modes.

The final precision of the extrapolation at a level of < 0.015 mag is ultimately defined by the standard deviation of the modes at a level of < 0.08 mag due to the medium fluctuations and by the number (27) of the independent modes: $0.08/27^{0.5} \approx 0.015$.

We should obtain the radial gradients of the dereddened colours and absolute magnitudes using radial gradients of age and metallicity. In the literature, no considerable radial age gradient is known in the thin layer under consideration. The estimate of the radial metallicity⁷ gradient

$$\Delta[\text{Fe}/\text{H}]/\Delta X' = -0.082 \text{ dex kpc}^{-1} \quad (13)$$

⁶ Hereafter we apply such a verification of our results using a resampling method in all cases when we calculate moving modes.

⁷ $[\text{Fe}/\text{H}]$ is the logarithmic Fe abundance relative to the Sun.

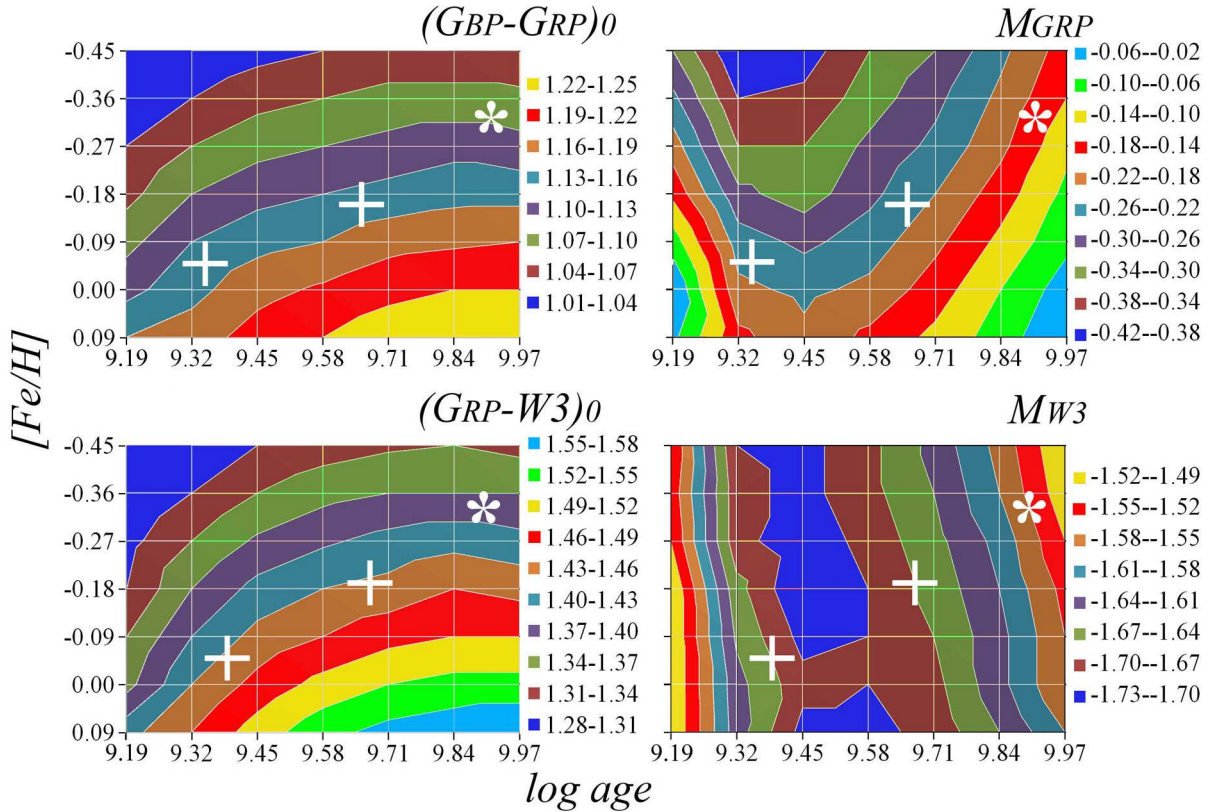


Figure 5. PARSEC predictions of the intrinsic colours and absolute magnitudes of the clump as functions of age and $[\text{Fe}/\text{H}]$. The solutions from Table 5 for the input from Table 4 are shown by the white crosses and stars for $Z = 0$ and $|Z| = 1700$ pc, respectively.

for the clump giants within $|Z| < 100$ and $-3500 < X' < 2000$ pc from Huang et al. (2015) seem to be the most appropriate for our subsample in the thin layer. Other estimates for such a gradient are within a few hundredths of dex kpc^{-1} from (13) (see, e.g. Önal Taş et al. 2016). A reasonable estimate of the median metallicity of clump giants at $X' = 0$ is $-0.10 < [\text{Fe}/\text{H}] < 0$ (Huang et al. 2015). In combination with gradient (13), this suggests that a reasonable estimate of the median metallicity in our thin layer is within the range

$$-0.16 < [\text{Fe}/\text{H}] < +0.06. \quad (14)$$

To convert a gradient of metallicity into gradients of the dereddened colours and absolute magnitudes, we should use some theoretical stellar evolution model estimates. They are based on theoretical isochrones in combination with colour versus effective temperature (T_{eff}) relations and bolometric corrections. We use the model estimates from PARSEC⁸, MIST⁹, and the Bag of Stellar Tracks and Isochrones (IAC-BaSTI, Hidalgo et al. 2018¹⁰). The predictions of the intrinsic colours and absolute magnitudes as functions of age

⁸ PARSEC version 1.2S with $[\alpha/\text{Fe}] = 0$, solar metallicity $Z = 0.0152$, mass-loss efficiency $\eta = 0.2$, where η is the free parameter in the Reimers' law (Reimers 1975).

⁹ MIST version 1.2 with $[\alpha/\text{Fe}] = 0$ and the reference protosolar metallicity $Z = 0.0142$.

¹⁰ <http://basti-iac.oa-abruzzo.inaf.it/index.html>. This IAC-BaSTI version assumes $[\alpha/\text{Fe}] = 0$, overshooting, diffusion, mass-loss efficiency $\eta = 0.3$. IAC-BaSTI does not provide any estimate for the W3 band.

and $[\text{Fe}/\text{H}]$ are presented in Fig. 5, 6 and 7 for PARSEC, MIST and IAC-BaSTI, respectively.

These predictions will be compared with our empirical estimates in Sect. 4.2.

We note that the different models provide fairly comparable predictions for $(G_{\text{BP}} - G_{\text{RP}})_0$ and M_{GRP} . In contrast, the PARSEC predictions for $(G_{\text{RP}} - W3)_0$ and M_{W3} are, respectively, systematically bluer and fainter by several hundredths of a magnitude than those from MIST. This is especially noticeable in the most interesting region $2.5 - 9.3$ Gyr and $-0.45 < [\text{Fe}/\text{H}] < 0.05$. We will discuss this in more detail in Sect. 4.2.

To estimate the gradients, we should consider a proper range of ages. Girardi (2016) notes that ‘in any galaxy with a relatively constant star-formation rate over gigayear scales, the mean age of the red clump will be relatively young and located, indicatively, somewhere between 1 and ~ 4 Gyr’. The upper limit is still rather uncertain. Therefore, we conservatively adopt it as 6 Gyr. Considering the lower limit, we must take into account the division of the clump giants into two main types (Girardi 2016). Low-mass clump giants have degenerate helium cores at the RGB stage, while the cores of high-mass clump giants are never completely degenerated. As a result, low-mass clump giants have similar masses of their helium cores at the stage of the helium nuclear fusion and, hence, similar colours and absolute magnitudes. This allows them to form a compact clump in HR diagrams. In contrast, high-mass clump giants have scattered helium core masses and, hence, scattered absolute magnitudes in HR diagrams. With slightly bluer colours w.r.t the low-mass clump giants, the high-mass clump giants form an additional ‘vertical structure’ at

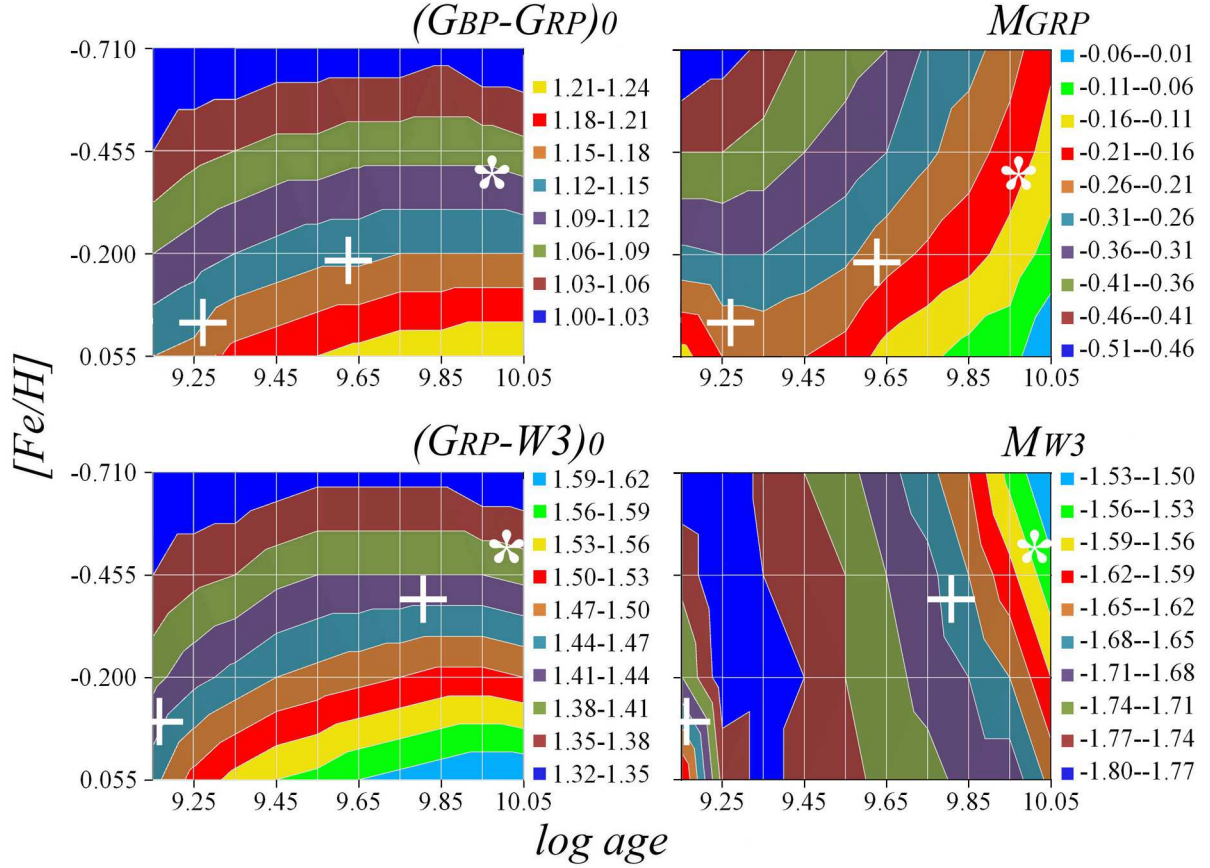


Figure 6. The same as Fig. 5 but for MIST.

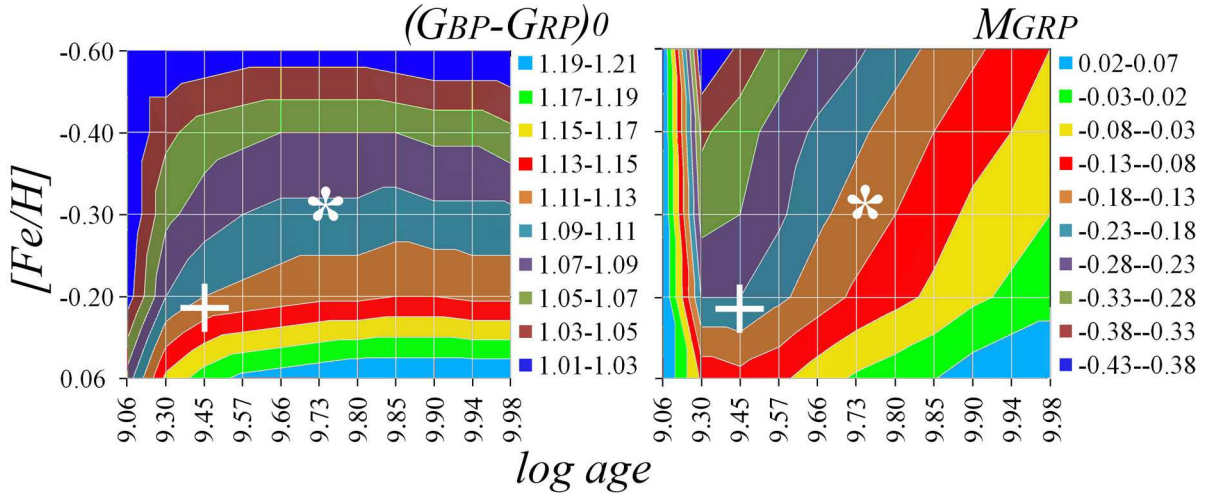


Figure 7. The same as Fig. 5 but for IAC-BaSTI.

the blue side of the main clump in a HR diagram, as discussed by Girardi (2016).

PARSEC, MIST and IAC-BaSTI consistently show that the high- and low-mass clump giants are separated by a mass value of 1.7 solar masses. Due to the correlation between mass and age for clump giants, this means a dominance of high-mass clump giants for an age $\lesssim 1.6$ Gyr ($\log age \lesssim 9.2$), their absence for an age $\gtrsim 2$ Gyr

($\log age \gtrsim 9.3$) and a mix of clump giants for an in-between age. Fig. 5, 6 and 7 confirm this: the colours and absolute magnitudes of the clump change significantly for $\log age < 9.3$ and, especially, for $\log age < 9.2$.

There are observational evidences (e.g. those summarized in Girardi 2016) that the low-mass clump giants certainly dominate in the clump domain of any HR diagram for the solar neighbour-

hood¹¹. Consequently, similar to the above-mentioned contamination by branch and asymptotic branch giants, a contamination by high-mass clump giants cannot affect the modes of the observables. These modes are completely defined by low-mass clump giants. Therefore, the median and mean age of the clump in the space under consideration must be within 1.6 – 6 Gyr ($9.20 < \log \text{age} < 9.78$). Hence, we consider the age range < 1.6 Gyr in Fig. 5, 6 and 7 only for illustrative purposes.

Fig. 5, 6 and 7 show that for gradient (13) within range (14) and a specific age within 1.6 – 6 Gyr these models provide rather consistent gradients of the dereddened colours and absolute magnitudes. Moreover, these gradients are rather small: only a few hundredths of a magnitude. For example, for 2.8 Gyr ($\log \text{age} = 9.45$), PARSEC gives $(G_{\text{BP}} - G_{\text{RP}})_0 = 1.15$ and 1.18 for $[\text{Fe}/\text{H}] = -0.09$ and -0.01 , respectively, and, finally, the colour gradient of 0.03 mag. For the same input, MIST gives $(G_{\text{BP}} - G_{\text{RP}})_0 = 1.17$ and 1.19 with a gradient of 0.02 mag, while IAC-BaSTI gives $(G_{\text{BP}} - G_{\text{RP}})_0 = 1.15$ and 1.17 with a gradient of 0.02 mag. Note that the radial gradients far from the Galactic mid-plane are even lower (Huang et al. 2015).

It is worth noting that the gradients of the dereddened colours and absolute magnitudes cannot be derived empirically by use of our data. The reason for that is that both dust volume density and metallicity tend to increase towards the Galactic Centre. Hence, the extinction, the reddening, as well as the dereddened colours and absolute magnitudes under consideration also tend to increase towards the Galactic Centre. The degeneracy of these quantities makes the uncertainty of any empirical estimate of the gradients unacceptable.

Therefore, we cannot estimate a differential extinction and reddening in the thin layer along X or X' , but only along Y , where we find no gradient.

However, in this paper we do not seek to study the differential reddening, but extrapolation of the observables to $R = 0$. To do this, we consider the observables as functions of R . In such a way, the gradients at negative and positive X' compensate each other. This results in a negligible contribution of the small theoretical gradients into our extrapolation, at a level < 0.01 mag within our thin layer. Therefore, we can ignore any radial gradient for the thin layer in this extrapolation. Consequently, any variation of an observable with R is considered as a result of reddening or extinction. Note that the extrapolation is performed at the expense of the averaging of the longitudinal variations of the observables.

The moving modes of the observables as functions of $(X^2 + Y^2)^{0.5}$ are shown in Fig. 8. Since the layer is thin, this figure would not change, if we use R instead of $(X^2 + Y^2)^{0.5}$.

Fig. 8 shows a distinct increase of all the modes with $(X^2 + Y^2)^{0.5}$ due to extinction or reddening, except $\text{mode}(M_{\text{W}3} + A_{\text{W}3})$. The latter shows no trend due to negligible variations of both $M_{\text{W}3}$ and $A_{\text{W}3}$.

The variations in Fig. 8 can be approximated by some simple functions to derive the dereddened colours, absolute magnitudes, extinctions and reddenings by use of equations (8)–(12).

We consider a cumulative extinction or reddening in a dust layer with an almost uniform dust distribution along the X - and Y -axes, and a nearly exponential distribution along the Z -axis. In this case, a simple simulation allows us to choose the approximation by a parabolic function of R or $(X^2 + Y^2)^{0.5}$, which saturates when coming out of the layer. This was first realized by Arenou, Grenon & Gomez (1992, hereafter AGG92) [their equation (5) and figure 1]. They approxi-

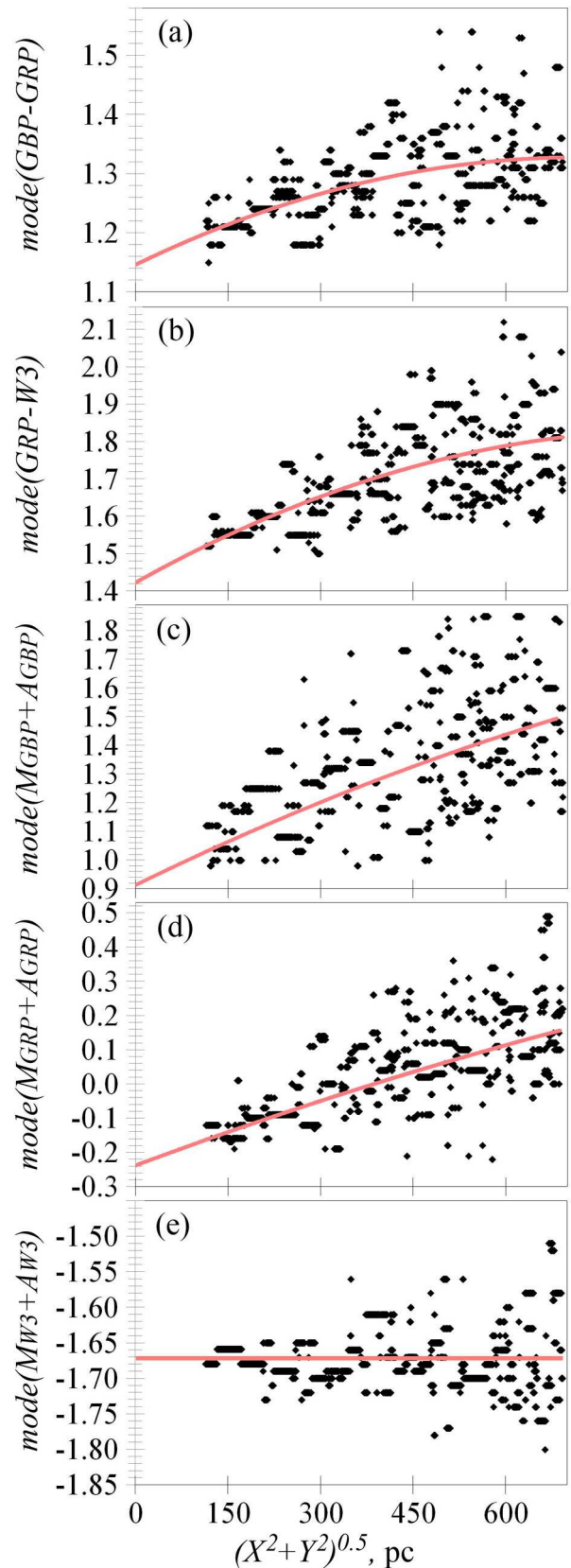


Figure 8. Moving modes of the observables, calculated with a window of 400 stars, as functions of $(X^2 + Y^2)^{0.5}$ for 10 802 stars with $|Z| < 40$ pc. The curves show approximations and extrapolations by parabolas.

¹¹ This may not be the case in some other regions of the Galaxy or in other galaxies. That is why Girardi (2016) sets the lower limit of the mean age of the clump at 1 Gyr.

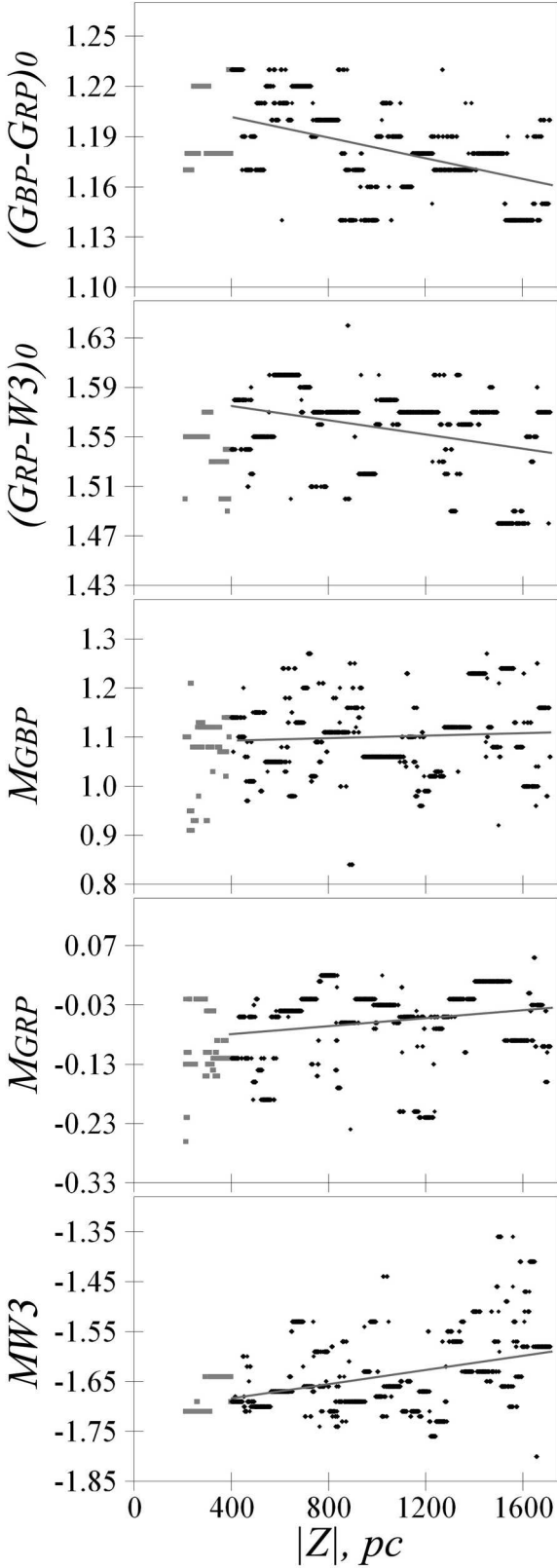


Figure 9. The modes of the dereddened colours and absolute magnitudes obtained by use of the reddening from MF15 and extinction law from WC19 for 5821 stars within $|b| > 68.75^\circ$. The modes for $|Z| < 400$ and $|Z| > 400$ pc are shown by grey and black symbols, respectively. The gradients for $|Z| > 400$ pc are shown by lines.

estimated the extinction in 199 celestial areas through some parabolas of R in their 3D extinction model.

The result of our approximation of the modes by parabolas and their extrapolation to $R = 0$ is presented in Table 2. As a by-product, we derive the following average extinctions and reddenings for $(X^2 + Y^2)^{0.5} = 700$ and $|Z| < 40$ pc as the differences between the values at $R = 0$ and $(X^2 + Y^2)^{0.5} = 700$ pc:

$$A_{\text{GBP}} = 1.50 \pm 0.015 - 0.91 \pm 0.015 = 0.59 \pm 0.02, \quad (15)$$

$$A_{\text{GRP}} = 0.16 \pm 0.015 - (-0.24 \pm 0.015) = 0.40 \pm 0.02, \quad (16)$$

$$A_{\text{W3}} = -1.67 \pm 0.015 - (-1.67 \pm 0.015) = 0.00 \pm 0.02, \quad (17)$$

$$E(G_{\text{BP}} - G_{\text{RP}}) = 1.34 \pm 0.015 - 1.15 \pm 0.015 = 0.19 \pm 0.02, \quad (18)$$

$$E(G_{\text{RP}} - W3) = 1.83 \pm 0.015 - 1.43 \pm 0.015 = 0.40 \pm 0.02. \quad (19)$$

Our empirical extinction law, written by results (15)–(19), can be compared with some other extinction laws. Given $A_{\text{GBP}} = 0.59$ mag, the extinction laws of Davenport et al. (2014, hereafter DIB14) for low latitudes¹², Schlafly et al. (2016, hereafter SMS16), and WC19 provide $A_{\text{GRP}} = 0.35, 0.35, 0.35$, $A_{\text{W3}} = 0.06, 0.03, 0.02$, $E(G_{\text{BP}} - G_{\text{RP}}) = 0.24, 0.24, 0.24$, and $E(G_{\text{RP}} - W3) = 0.31, 0.32, 0.33$ mag, respectively. The widely used extinction law by Cardelli, Clayton & Mathis (1989, hereafter CCM89) does not provide A_{W3} . However, for $A_{\text{GBP}} = 0.59$ mag the CCM89 extinction law with $R_V \equiv A_V/E(B - V) = 3.1$ gives $A_{\text{GRP}} = 0.37$ and $E(G_{\text{BP}} - G_{\text{RP}}) = 0.22$ mag in best agreement with our extinction law.

We derive the colour excess ratios (CERs) $E(G_{\text{RP}} - W3)/E(G_{\text{BP}} - G_{\text{RP}}) = 2.11^{+0.35}_{-0.30}, 1.24, 1.28$, and 1.33 , from our results and the laws by DIB14 for low latitudes, SMS16, and WC19, respectively.

It is seen that these extinction laws differ in their predictions for A_{W3} . Our extinction law deviates from the remaining ones, but no more than 3σ . This deviation can be explained by our averaging of the longitudinal variations of the observables.

Result (15) corresponds to $A_V/R = 0.83, 0.82, 0.82, 0.84$ mag kpc^{-1} by use of the extinction laws by CCM89 with $R_V = 3.1$, DIB14 for low latitudes, SMS16, and WC19, respectively. Similarly, result (16) corresponds to $A_V/R = 0.87, 0.94, 0.95, 0.97$, respectively. The average is $A_V/R = 0.88 \pm 0.07$ mag kpc^{-1} . It is worth noting that this estimate is averaged over the longitude. Hence, this reflects the differential reddening along Y rather than along X' , where the gradients of the observables are high. This may be a reason why this estimate is lower than common estimates along the mid-plane, e.g. $1.1 < A_V/R < 1.7$ mag kpc^{-1} of Vergely et al. (1998, and references therein). The averaging of the longitudinal variations of the observables makes our estimates (15)–(19) less robust and important than the extrapolated estimates of the dereddened colours and absolute magnitudes in Table 2.

¹² DIB14 provide different extinction laws for low and high-latitudes. The study of DIB14 is very important as the only direct comparison of the empirical extinction laws in the Galactic disc and halo: see their table 3 and figures 6 and 7.

Table 2. The modes of the observables in a thin layer of $|Z| < 40$ pc approximated by parabolas and extrapolated to $R = 0$. The uncertainty of all the mode values is 0.015 mag.

$(X^2 + Y^2)^{0.5}$, pc	$mode(M_{G_{BP}} + A_{G_{BP}})$	$mode(M_{G_{RP}} + A_{G_{RP}})$	$mode(M_{W3} + A_{W3})$	$mode(G_{BP} - G_{RP})$	$mode(G_{RP} - W3)$
0	0.91	-0.24	-1.67	1.15	1.43
700	1.50	0.16	-1.67	1.34	1.83

3.2 Vertical gradients

We estimate the vertical gradients of the intrinsic colours and absolute magnitudes in a space beyond the dust layer. There must be no variations of the cumulative reddening in such a space along each line of sight. However, such a space maintains some small variations of the cumulative reddening from one line of sight to another due to medium fluctuations between these lines of sight inside the dust layer. Moreover, lines of sight far from the Galactic poles cross rather dense regions of the dust layer. Hence, we must only consider some neighbourhood of the poles.

We consider a subsample of 5821 stars within the vertical cones resting on the base of the space cylinder under consideration, i.e. with $|b| > 90^\circ - \arctan(700/1800) \approx 68.75^\circ$. We consider a space with $|Z| > 400$ pc as one with a negligible increase of the reddening along $|Z|$. Indeed, any reasonable vertical distribution of dust suggests such an increase by only < 12 per cent.

The observables of each star must be corrected for reddening and extinction through the whole dust half-layer. Therefore, we should adopt some estimates of the reddening or extinction from us to infinity, i.e. taken from a 2D reddening map. We use one of the most accurate 2D reddening maps of [Meisner & Finkbeiner \(2015\)](#), hereafter MF15). It is based on the observations of the dust emission in the far-IR by *Planck* and a reddening-to-emission calibration. In Sect. 5 we discuss that this map may have some systematic errors. However, here we do not need very accurate estimates of the reddening and/or extinction across the dust layer, since they are nearly cancel each other out in the colour and magnitude gradients outside the layer.

Note that 3D reddening/extinction maps and models are not useful in studying the vertical gradients, since, usually, they do not extend far enough from the Galactic mid-plane. For example, the 3D maps by [Lallement et al. \(2019\)](#), hereafter LVV19)¹³ and [Gontcharov \(2017a\)](#), hereafter G17) extend up to only $|Z| < 400$ and 600 pc, respectively. Only the 3D reddening maps by [DCL03](#) and [Green et al. \(2019\)](#), hereafter GSF19)¹⁴ extend far enough. However, they have some drawbacks: [DCL03](#) has a lower angular resolution, while [GSF19](#) covers only part of the sky. Yet, we check that the use of [DCL03](#) or [GSF19](#) provides us with vertical gradients, which are the same as using [MF15](#) within 0.01 mag kpc^{-1} .

The moving modes of the dereddened colours and absolute magnitudes, with a window of 400 stars along $|Z|$, as functions of $|Z|$, are presented in Fig. 9. We derive the following vertical gradients (in mag kpc^{-1}) for $400 < |Z| < 1714$ pc:

$$\Delta(G_{BP} - G_{RP})_0 / \Delta|Z| = -0.03 \pm 0.01, \quad (20)$$

$$\Delta(G_{RP} - W3)_0 / \Delta|Z| = -0.03 \pm 0.01. \quad (21)$$

¹³ <http://stilism.obspm.fr>

¹⁴ <http://argonaut.skymaps.info/>

$$\Delta M_{G_{BP}} / \Delta|Z| = +0.01 \pm 0.01, \quad (22)$$

$$\Delta M_{G_{RP}} / \Delta|Z| = +0.04 \pm 0.01, \quad (23)$$

$$\Delta M_{W3} / \Delta|Z| = +0.07 \pm 0.01, \quad (24)$$

The uncertainties of these gradients are computed as standard deviations of the gradients calculated when the space under consideration is varied in the range $400 < |Z| < 600$ pc, $60 < |b| < 75^\circ$.

The modes within $|Z| < 400$ pc are shown in Fig. 9 by grey symbols. They allow us to suggest that their gradients within $|Z| < 400$ pc are similar to those within $|Z| > 400$ pc.

3.3 The narrow vertical cylinder

We analyse the modes of the observables as functions of Z in a narrow space cylinder of $(X^2 + Y^2)^{0.5} < 80$ pc. This allows us to estimate the intrinsic colours and absolute magnitudes of the nearby clump giants. Then we can compare them with the values extrapolated in the thin coordinate layer in Sect. 3.1. Also, we can compare the observables near the Sun with those at high $|Z|$, behind the whole dust half-layer. This allows us to derive the extinctions and reddenings through the whole dust half-layer.

The radius of the cylinder is set so that near the Sun it is limited by the Local Bubble. A wider cylinder may be contaminated by reddened stars. The cylinder contains 1224 stars. It is enough to calculate rather precise modes of the observables for only three ranges of Z . They are presented in Table 3. Each range contains 408 stars. The asymmetry of the ranges w.r.t. $Z = 0$ is due to an uneven spatial distribution of the stars along Z . The differences between the values at $Z = -384$ and $Z = +304$ pc is due to an offset of the Sun w.r.t. the dust layer mid-plane: more dust is below than above the Sun.

The stars in the range $(X^2 + Y^2)^{0.5} < 80$, $-168 < Z < +114$ pc can be considered as unreddened ones. More precisely, any reasonable distribution of dust suggests their average reddening to be $E(B-V) < 0.01$ mag. This is negligible w.r.t. the uncertainties which we consider further.

Table 4 presents our estimates of the giant clump dereddened colours and absolute magnitudes for $Z = 0$. These are averaged estimates for $R = 0$ from Table 2 and for $Z = 0$ from Table 3. Note that these estimates are in perfect agreement with each other. Their uncertainty 0.01 mag is based on the assumption that they are independent. Also, Table 4 contains our estimates for $|Z| = 1700$ pc, which are based on the estimates for $Z = 0$ and vertical gradients (20)–(24), which are calculated within $400 < |Z| < 1714$ pc. The uncertainty ± 0.02 includes the uncertainty of the gradients added in quadrature to the uncertainty at $Z = 0$. We compare Table 4 with the theoretical estimates in Sect. 4.2.

Any reasonable vertical distribution of dust suggests that > 80

Table 3. The modes of the observables in a narrow cylinder of $(X^2 + Y^2)^{0.5} < 80$ pc. The uncertainty of all the mode values is 0.015 mag.

Z range, pc	Median Z, pc	$mode(M_{G_{BP}} + A_{G_{BP}})$	$mode(M_{G_{RP}} + A_{G_{RP}})$	$mode(M_{W_3} + A_{W_3})$	$mode(G_{BP} - G_{RP})$	$mode(G_{RP} - W_3)$
-1724 – -168	-384	1.13	-0.09	-1.62	1.22	1.53
-168 – +114	-40	0.91	-0.23	-1.67	1.14	1.44
+114 – +1723	+304	1.09	-0.11	-1.64	1.20	1.53

Table 4. Our estimates of the giant clump dereddened colours and absolute magnitudes.

$ Z $, pc	$mode(M_{G_{BP}})$	$mode(M_{G_{RP}})$	$mode(M_{W_3})$	$mode[G_{BP} - G_{RP}]_0$	$mode[G_{RP} - W_3]_0$
0	0.910 ± 0.01	-0.235 ± 0.01	-1.670 ± 0.01	1.145 ± 0.01	1.435 ± 0.01
1700	0.927 ± 0.02	-0.167 ± 0.02	-1.551 ± 0.02	1.094 ± 0.02	1.384 ± 0.02

per cent of the cumulative reddening or extinction to infinity should manifest in modes of the observables for the outer ranges of the vertical cylinder. This leads to a negligible systematic underestimation $\Delta E(B - V) < 0.012$ mag of the reddening across the whole dust half-layer, if this reddening is $E(B - V) < 0.06$ mag. Therefore, the ranges of the vertical cylinder are convenient to derive the differences of the observables between the nearby stars and the stars behind the dust layer.

Hence, we estimate the extinctions and reddenings across the whole dust half-layer as the differences between the values for $Z = -40$ and the average values for $Z = -384$ and 304 pc from Table 3. The values for $Z = -384$ and 304 pc must be corrected for vertical gradients (20)–(24) in the interval $\Delta|Z| = (|-384 - (-40)| + |304 - (-40)|)/2 = 344$ pc. The reddening and extinction estimates are as follows:

$$A_{G_{BP}} = (1.13 + 1.09)/2 - (0.91 + 0.01 \cdot 0.344) = 0.20 \pm 0.02, \quad (25)$$

$$A_{G_{RP}} = (-0.09 - 0.11)/2 - (-0.23 + 0.04 \cdot 0.344) = 0.12 \pm 0.02, \quad (26)$$

$$A_{W_3} = (-1.62 - 1.64)/2 - (-1.67 + 0.07 \cdot 0.344) = 0.016 \pm 0.02, \quad (27)$$

$$E(G_{BP} - G_{RP}) = (1.22 + 1.20)/2 - (1.14 - 0.03 \cdot 0.344) = 0.08 \pm 0.02, \quad (28)$$

$$E(G_{RP} - W_3) = (1.53 + 1.53)/2 - (1.44 - 0.03 \cdot 0.344) = 0.10 \pm 0.02. \quad (29)$$

Estimates (25), (26), (28), and (29) correspond to $E(B - V) \approx 0.06$ mag by use of all the extinction laws by DIB14 for high-latitudes, SMS16 and WC19. Estimate (27) corresponds to very different $E(B - V)$ by use of the different laws: 0.048, 0.082, and 0.127 mag with the laws by DIB14 for high-latitudes, SMS16 and WC19, respectively.

Results (25)–(29) define our extinction law. It is consistent with all the laws mentioned above. This is seen from the following direct comparison. Given $A_{G_{BP}} = 0.2$, the extinction laws by DIB14 for high-latitudes, SMS16 and WC19 provide $A_{G_{RP}} = 0.12$, 0.12, 0.12 and $A_{W_3} = 0.02$, 0.01, 0.01 mag, respectively, which are in good agreement with estimates (26) and (27). The A_{W_3} estimate from DIB14 for high-latitudes is in best agreement with our estimate. Given $A_{G_{BP}} = 0.2$, the extinction law by CCM89 with $R_V = 3.1$ provides $A_{G_{RP}} = 0.13$.

Estimates (25)–(29) provide the CER $1.25^{+0.75}_{-0.45}$ in good agreement with the CERs, which are mentioned in Sect. 3.1 for the other laws.

Estimates (25)–(29) are important, being independent of any model and based only on the differences in the observables between the nearby giants and those behind the dust layer. We suppose that there is no other interpretation of these differences, except for the extinction/reddening across the whole dust half-layer. These estimates will be compared with some other estimates in Sect. 5.

Our estimate (27) of the IR extinction is quite uncertain. However, in combination with nearly zero IR extinction (17) in the thin layer, this does not contradict the variation of the extinction law with $|Z|$ or latitude, which has been found by DIB14 and Gontcharov (2012a, 2013, 2016a). These studies use a multiband photometry for stars up to $|Z| = 25$ kpc. They reveal a similar increase of the infrared-to-optical extinction ratios with $|Z|$ or latitude (see figure 9 in Gontcharov 2016a). This needs to be further explored, based on some more accurate IR extinction estimates.

4 DISCUSSION

4.1 Absolute magnitudes

Both $(G_{BP} - G_{RP})_0$ and $M_{G_{RP}}$ show an increase with age and $[Fe/H]$, as seen in Fig. 5, 6, and 7. This leads to a dependence of $M_{G_{RP}}$ on this colour. Such a dependence of clump absolute magnitudes on its colours in the optical range is well known (Girardi 2016). This makes it difficult to use the clump as a ‘standard candle’ in the optical range.

In contrast, $(G_{RP} - W_3)_0$ increases mostly with $[Fe/H]$, while M_{W_3} – mostly with age, as seen in Fig. 5 and 6. Hence, M_{W_3} is nearly independent of $(G_{RP} - W_3)_0$. This must be more or less true for all IR absolute magnitudes and colours of the clump. Therefore, the IR absolute magnitudes of the clump seem to be suitable for using the clump as a ‘standard candle’. However, Fig. 5 and 6 show a strong dependence of M_{W_3} on age. Unfortunately, age is a poorly known quantity, especially, with its variations with $|Z|$, X' and from one galaxy to another. Yet, to use the clump as a ‘standard candle’ in the IR range, one must take into account a relation between age and absolute magnitude of the clump (see the discussion in Chen et al. 2017).

Ignoring such a relation may be a reason for the inconsistency of the empirical estimates of the IR absolute magnitudes. The most recent and precise estimates of M_{W_3} near the Sun are as follows:

$$\begin{aligned} & -1.552 \pm 0.020; \\ & -1.585 \pm 0.019; \end{aligned}$$

-1.606 ± 0.024 obtained by [Yaz Gökçe et al. \(2013\)](#) for the fractional parallax < 0.05 , < 0.10 , and < 0.15 , respectively;
 -1.638 ± 0.011 ([RBA18](#)) (we discuss this result in Sect. 5);
 -1.676 ± 0.028 obtained by [Yaz Gökçe et al. \(2013\)](#) via the transformation from the 2MASS to the WISE photometric system;
 -1.752 ± 0.068 ([Chen et al. 2017](#));
 -1.67 ± 0.02 ([Hawkins et al. 2017](#));
 -1.66 ± 0.02 ([Gontcharov 2017b](#));
 and our estimate
 -1.67 ± 0.01 .

Note that the latter is based on the most complete sample.

The first four estimates deviate from each other and from the remaining estimates. The last five estimates agree with each other and with the value -1.68 at a level of 1σ . However, this agreement may be illusive, since some of these studies seem to ignore the dependences of M_{W3} on age and $|Z|$.

We put these estimates on the theoretical diagrams in Fig. 5 and 6. We find unreliable estimates of age and/or $[\text{Fe}/\text{H}]$ for the first three estimates of M_{W3} by use of both PARSEC and MIST. The reason of the deviation of the first three results is unknown.

The deviation of the result of [RBA18](#) can be explained by a rather high $|Z|$ of their sample. The median $|Z|$, mean $|Z|$, and standard deviation of $|Z|$ for their sample are 208, 206 and 85 pc, respectively. [RBA18](#) assume $A_{W3} = 0$ for their sample and, consequently, $M_{W3} + A_{W3} = M_{W3} = -1.638$ mag. The same $M_{W3} + A_{W3} \approx -1.64$ mag can be obtained from our estimates $M_{W3} = -1.67$, (24) and (27) followed by the median $M_{W3} = -1.655$ and $A_{W3} \approx 0.013$. Thus, the gradient of the absolute magnitude along $|Z|$ and the non-zero extinction can reconcile the estimate of [RBA18](#) with the majority of the empirical estimates.

Among all the estimates of M_{W3} , only the estimate of [Chen et al. \(2017\)](#) provides a reliable age and $[\text{Fe}/\text{H}]$ by use of MIST. The inconsistency of the most empirical estimates of M_{W3} with MIST seems to indicate an imperfection of the MIST predictions rather than an error in the empirical estimates. The estimate of [Chen et al. \(2017\)](#) can be closer to the remaining empirical estimates. [Chen et al. \(2017\)](#) use the rather large extinction coefficient $A_{W3}/E(B-V) = 0.349$ to correct the result for A_{W3} . For comparison, the extinction laws by [DIB14](#) for low latitudes, [SMS16](#) and [WC19](#) provide $A_{W3}/E(B-V) = 0.339$, 0.195, and 0.126, respectively. With the latter, [Chen et al. \(2017\)](#) would obtain M_{W3} several hundredths of a magnitudes fainter, i.e. in better agreement with the bulk of the above estimates.

4.2 Our results versus theoretical isochrones

Table 4 provides the empirical positions of the giant clump in the HR diagrams ‘ $(G_{\text{BP}} - G_{\text{RP}})_0$ versus M_{GRP} ’ and ‘ $(G_{\text{RP}} - W3)_0$ versus M_{W3} ’. We convert these positions into age and metallicity of the clump by use of the theoretical relations in Fig. 5, 6 and 7. The positions for $Z = 0$ and $|Z| = 1700$ pc are shown in these figures by the white crosses and stars, respectively. The derived solutions, i.e. the pairs of the age and $[\text{Fe}/\text{H}]$, are shown in Table 5. Also, Table 5 presents the vertical gradients of the age and $[\text{Fe}/\text{H}]$. They are calculated from the differences of the age and $[\text{Fe}/\text{H}]$ for $Z = 0$ and $|Z| = 1700$ pc.

The uncertainties of the derived $\log \text{age}$ and $[\text{Fe}/\text{H}]$ are ± 0.05 and ± 0.06 dex, respectively. To calculate them, we take into account the uncertainties of the dereddened colours and absolute magnitudes from Table 4.

In some cases we find two solutions for $Z = 0$. They are shown by two crosses in one plot. Consequently, two gradients are calculated in such cases. The secondary solutions, i.e. those with a higher age

and lower $[\text{Fe}/\text{H}]$, are given in Table 5 in brackets. In the framework of the generally accepted theory of the giant clump ([Girardi 2016](#)), the secondary solutions seem to be less reliable w.r.t. the primary ones. Moreover, the secondary solutions are accompanied by the unrealistically low metallicities, as seen in Table 5.

Table 5 shows an acceptable agreement of our results, except for the MIST predictions for $(G_{\text{RP}} - W3)_0$ versus M_{W3} . The primary and secondary MIST age solutions for $Z = 0$ and $(G_{\text{RP}} - W3)_0$ versus M_{W3} (1.5 and 6.5 Gyr) are out of the reliable age range (1.6 – 6 Gyr) defined in Sect. 3.1. Moreover, the MIST isochrone for 1.5 Gyr is a typical isochrone of high-mass clump giants. Consequently, MIST claims that high-mass clump giants dominate in our sample for $Z = 0$. This seems unlikely, as discussed in Sect. 3.1. The most important here is the discrepancy between the MIST estimates for $(G_{\text{BP}} - G_{\text{RP}})_0$ versus M_{GRP} and $(G_{\text{RP}} - W3)_0$ versus M_{W3} . This may indicate an issue in the MIST predictions for $W3$. Most likely, this is an issue in the colour- T_{eff} relation and/or bolometric correction used.

We average the primary estimates for $(G_{\text{BP}} - G_{\text{RP}})_0$ versus M_{GRP} and conclude with caution that age and $[\text{Fe}/\text{H}]$ of the clump change from 2.3 ± 0.5 to 7.8 ± 2.2 Gyr and from -0.08 ± 0.08 to -0.34 ± 0.06 , respectively, when $|Z|$ changes from 0 to 1700 pc. Consequently, the vertical gradients of the age and $[\text{Fe}/\text{H}]$ are 3.2 ± 1.6 Gyr kpc^{-1} and -0.16 ± 0.07 dex kpc^{-1} , respectively.

Our age gradient agrees with an estimate of 4 Gyr kpc^{-1} by [Casagrande et al. \(2016\)](#). Moreover, the vertical gradients of M_{W3} and age along $|Z|$ are combined into the vertical gradient of M_{W3} along age $0.02^{+0.03}_{-0.01}$ mag Gyr^{-1} . This agrees with its estimate 0.017 ± 0.004 mag Gyr^{-1} by [Chen et al. \(2017\)](#).

Our $[\text{Fe}/\text{H}]$ gradient is in the middle of the diversity of its estimates presented, for example, by [Önal Taş et al. \(2016\)](#). In particular, our $[\text{Fe}/\text{H}]$ gradient agrees with the estimate -0.15 ± 0.01 dex kpc^{-1} by [Huang et al. \(2015\)](#) for a large sample of clump giants within $-1 < X' < 1$ and $|Z| < 3$ kpc. However, our $[\text{Fe}/\text{H}]$ gradient disagrees with the estimate -0.31 ± 0.03 dex kpc^{-1} by [Soubiran et al. \(2008\)](#) for a small sample of local clump giants.

Our results can be applied to some contradictory cases. [RBA18](#) attempt to create a sample of clump giants with a very low reddening of $E(B-V) < 0.015$ mag. They select stars with reddening estimates from the 2D reddening map of [SFD98](#) and other maps with very low estimates of reddening far from the Galactic mid-plane. [RBA18](#) obtain the median $E(B-V) = 0.01$ mag for their sample. The majority of their giants are located at high $|Z|$. For their median $|Z| = 208$ pc, our results by use of PARSEC suggest a median age of about 3 Gyr and the median $[\text{Fe}/\text{H}] = -0.08$. [RBA18](#) claim that the position of their sample in the HR diagram with the $G - K_s$ colour ‘seems to nicely fit’ a PARSEC isochrone. However, their figure 8 shows that the location of the clump better fits an isochrone of 5 Gyr and $[\text{Fe}/\text{H}] = 0$. This PARSEC isochrone is $\Delta(G - K_s) = 0.1$ mag redder than the isochrone for 3 Gyr and $[\text{Fe}/\text{H}] = -0.08$. Thus, there are two competing sets of the parameters to fit the observed clump by a PARSEC isochrone: [RBA18](#)’s 5 Gyr, $[\text{Fe}/\text{H}] = 0$, $E(B-V) = 0.01$ mag versus our 3 Gyr, $[\text{Fe}/\text{H}] = -0.08$ and a much higher reddening.

To estimate the latter, we must accept the isochrone colour difference $\Delta(G - K_s) = 0.1$ mag as the difference $\Delta E(G - K_s) = 0.1$ mag between the reddening estimates. It is converted to $\Delta E(B-V) = 0.044$ by use of the extinction law by [WC19](#). Hence, the needed, much higher reddening is $E(B-V) = 0.01 + 0.044 = 0.054$ mag. This is in perfect agreement with our estimate of the median reddening at $|Z| = 208$ pc. Finally, our set of the parameters, i.e. 3 Gyr, $[\text{Fe}/\text{H}] = -0.08$, and $E(B-V) = 0.054$ mag, better corresponds to

Table 5. Age, [Fe/H] and their vertical gradients derived for the pairs $(G_{BP} - G_{RP})_0 - M_{GRP}$ and $(G_{RP} - W3)_0 - M_{W3}$ from Table 4 by use of different models. The secondary solutions are given in brackets.

Model	Age / [Fe/H]	Z	$(G_{BP} - G_{RP})_0$ versus M_{GRP}	$(G_{RP} - W3)_0$ versus M_{W3}
PARSEC	Age	Z = 0	$2.2^{+0.3}_{-0.2}$ ($4.6^{+0.6}_{-0.5}$) Gyr	$2.5^{+0.3}_{-0.3}$ ($4.7^{+0.6}_{-0.5}$) Gyr
		Z = 1700 pc	$8.3^{+1.0}_{-0.9}$ Gyr	$7.8^{+1.0}_{-0.8}$ Gyr
		gradient	$3.6^{+1.0}_{-0.9}$ ($2.2^{+1.2}_{-1.0}$) Gyr kpc ⁻¹	$3.1^{+1.0}_{-0.9}$ ($1.8^{+1.1}_{-1.0}$) Gyr kpc ⁻¹
PARSEC	[Fe/H]	Z = 0	-0.05 ± 0.06 (-0.16 ± 0.06)	-0.05 ± 0.06 (-0.19 ± 0.06)
		Z = 1700 pc	-0.32 ± 0.06	-0.33 ± 0.06
		gradient	-0.16 ± 0.08 (-0.09 ± 0.08) dex kpc ⁻¹	-0.16 ± 0.08 (-0.08 ± 0.08) dex kpc ⁻¹
MIST	Age	Z = 0	$1.9^{+0.2}_{-0.2}$ ($4.3^{+0.5}_{-0.5}$) Gyr	$1.5^{+0.2}_{-0.2}$ ($6.5^{+0.8}_{-0.7}$) Gyr
		Z = 1700 pc	$9.4^{+1.1}_{-1.0}$ Gyr	$10.3^{+1.3}_{-1.1}$ Gyr
		gradient	$4.4^{+1.2}_{-1.0}$ ($3.0^{+1.3}_{-1.1}$) Gyr kpc ⁻¹	$5.2^{+1.3}_{-1.1}$ ($2.2^{+1.5}_{-1.3}$) Gyr kpc ⁻¹
MIST	[Fe/H]	Z = 0	-0.03 ± 0.06 (-0.18 ± 0.06)	-0.14 ± 0.06 (-0.39 ± 0.06)
		Z = 1700 pc	-0.40 ± 0.06	-0.52 ± 0.06
		gradient	-0.22 ± 0.08 (-0.13 ± 0.08) dex kpc ⁻¹	-0.22 ± 0.08 (-0.08 ± 0.08) dex kpc ⁻¹
IAC-BaSTI	Age	Z = 0	$2.8^{+0.3}_{-0.3}$ Gyr	
		Z = 1700 pc	$5.6^{+0.7}_{-0.6}$ Gyr	
		gradient	$1.6^{+0.8}_{-0.7}$ Gyr kpc ⁻¹	
IAC-BaSTI	[Fe/H]	Z = 0	-0.16 ± 0.06	
		Z = 1700 pc	-0.31 ± 0.06	
		gradient	-0.09 ± 0.08 dex kpc ⁻¹	

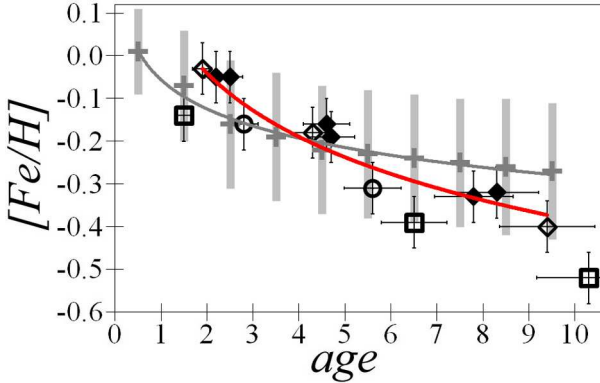


Figure 10. AMR by use of our results from Table 5: the PARSEC estimates – black filled diamonds, the MIST estimates for $(G_{BP} - G_{RP})_0$ versus M_{GRP} – black open diamonds, the MIST estimates for $(G_{RP} - W3)_0$ versus M_{W3} – the black open squares, and the IAC-BaSTI estimates – the black open circles. The approximation of the estimates for $(G_{BP} - G_{RP})_0$ versus M_{GRP} – the red curve. AMR from Soubiran et al. (2008) – the grey crosses with the wide error bars and the grey logarithmic approximating curve.

the PARSEC’s description of the giant clump than the set of RBA18. In this case, only a few giants in the sample of RBA18 actually have $E(B - V) < 0.015$ mag. This may be a typical case when the reddening far from the Galactic mid-plane is underestimated because slightly reddened stars are erroneously considered as unreddened. Also, this case demonstrates that one should not consider stars as unreddened, based only on their low reddening estimates in a map, without a detailed investigation of this issue.

4.3 Age–metallicity relation

We can derive the AMR in the vertical space cylinder. All our estimates from Table 5 are shown in Fig. 10 by different black symbols. The MIST estimates for $(G_{RP} - W3)_0$ versus M_{W3} (the open squares), the IAC-BaSTI estimates (the open circles) and the remaining estimates show slightly different trends: $[Fe/H] = -0.08 - 4.4 \times 10^{-11} \cdot age$, $[Fe/H] = -0.01 - 5.4 \times 10^{-11} \cdot age$, and $[Fe/H] = +0.05 - 4.8 \times 10^{-11} \cdot age$, respectively. The former seems to be unreliable, since it predicts too low metallicity for newborn stars. Thus, the MIST estimates for $(G_{RP} - W3)_0$ versus M_{W3} appear outliers in Fig. 10, as in Table 5. The remaining estimates show good agreement with each other, as for the different models, as for the primary or secondary solutions. It is worth noting that our estimates are model dependent. Hence, this agreement shows a convergence of the models for the optical bands. For the $(G_{BP} - G_{RP})_0$ versus M_{GRP} estimates the logarithmic approximation $[Fe/H] = 4.56 - 0.495 \log age$ is the most reliable. It is shown by the red curve. As seen from Fig. 10, it satisfies all the estimates within their uncertainties, except the MIST estimates for $(G_{RP} - W3)_0$ versus M_{W3} .

For comparison, the AMR from Soubiran et al. (2008) for a smaller sample of local clump giants is shown in Fig. 10 by the grey crosses with the wide error bars. Its logarithmic approximation is shown by the grey curve. It is seen that our results are more precise due to a larger sample. Our AMR is steeper, but consistent with that of Soubiran et al. (2008) within the uncertainties.

5 REDDENING ACROSS THE WHOLE DUST LAYER

Table 6 summarizes some estimates of the reddening across the whole dust half-layer below or above the Sun. In perfect agreement with the estimate of Gontcharov & Mosenkov (2018), mentioned in Sect. 1, the estimates from this study converge to $E(B - V) = 0.06$

Table 6. The estimates of the extinction or reddening across the whole dust half-layer below or above the Sun.

Model / map / result	Original estimate	$E(B - V)$ by DIB14
This study, narrow cylinder	$A_{\text{GBP}} = 0.20$	0.060
This study, narrow cylinder	$A_{\text{GRP}} = 0.12$	0.060
This study, narrow cylinder	$A_{\text{W3}} = 0.016$	0.048
This study, narrow cylinder	$E(G_{\text{BP}} - G_{\text{RP}}) = 0.08$	0.060
This study, narrow cylinder	$E(G_{\text{RP}} - W3) = 0.10$	0.061
Model AGG92	$A_{\text{V}} = 0.100$	0.031
Model DCL03	$E(B - V) = 0.018$	0.018
Model G12	$A_{\text{V}} = 0.214$	0.066
2D map SFD98	$E(B - V) = 0.018$	0.018
2D map MF15	$E(B - V) = 0.015$	0.015
3D map G17	$E(J - K_s) = 0.03$	0.060
3D map LVV19	$E(B - V) = 0.010$	0.010
3D map GSF19	$E(B - V) = 0.051$	0.051

mag¹⁵. The only exception is A_{W3} . However, it is rather uncertain, and its conversion to $E(B - V)$ strongly depends on an extinction law applied. The extinction law by **DIB14** for high-latitudes appears to be the most reliable in this case.

We do not provide uncertainties on the estimates in Table 6, since some of the estimates (i) are upper or lower limits without any uncertainty estimate (e.g. **AGG92**¹⁶), (ii) have very different estimates of their uncertainties from different studies (e.g. **SFD98**), or (iii) are, apparently, underestimated or overestimated. Anyway, the formal uncertainties of the estimates in Table 6 make little sense, since they cannot explain the large diversity of the estimates. In particular, Table 6 shows several widely used estimates of $E(B - V) \ll 0.06$, in contrast to our estimates.

Gontcharov & Mosenkov (2018) suggest some reasons of possible underestimation of the reddening across the whole dust half-layer in **SFD98** and **MF15**. Moreover, there is a lot of previous findings of this underestimation (a review is given by **Gontcharov 2016b**). For example, **Berry et al. (2012)** note: ‘It is confirmed beyond doubt that there are some systematic problems with the normalization¹⁷ of SFD extinction map’. **GSF19** note: ‘Both this work and **Green et al. (2018)** have identified systematic trends in reddening when comparing with the Planck14 and SFD dust maps, particularly for reddenings of $E(g - r) \lesssim 0.1$ mag. These systematics could be due to the uncertain zero-point of the dust reddening (e.g., what is the absolute reddening of some reference point on the sky?) and variation in R_{V} across the high-Galactic-latitude sky.’

The uncertainty of high reddenings in **SFD98** is 16 per cent. However, it is much worse for $E(B - V) \lesssim 0.1$ mag, as admitted by the authors. This uncertainty can be estimated from the standard deviation of the reddening-to-emission calibration residuals as ± 0.028 mag. Moreover, by use of *counts* of galaxies at high-latitudes, **SFD98** obtain approximately twice larger reddening-to-emission calibration coefficient than that obtained by use of the *reddened colours* of these galaxies. The latter coefficient is finally adopted in **SFD98**. This may lead to a systematic underestimation of the reddening across the

whole dust layer by use of the adopted calibration at a level of a few hundredths of a magnitude.

MF15 may also suffer from some reddening-to-emission calibration errors. In their figure 11, bottom left, **MF15** show a systematic trend in the calibration as a function of hot dust temperature. This trend suggests at least ± 0.02 mag systematic uncertainty of the calibration. This may lead to a similar systematic underestimation of the reddenings.

The similarity of the **DCL03** and **SFD98** estimates in Table 6 is defined by the method of the former: the **DCL03**’s ‘rescaling factors for latitudes $|b| > 30^\circ$ are based on the **SFD98** Galactic extinction map’ (**DCL03**).

Thus, **LVV19** seems to be the only recent all-sky 3D reddening map with very low estimates of the reddening across the whole dust half-layer. Possible systematic errors of **LVV19** due to some biases have been discussed by **Gontcharov & Mosenkov (2019)**.

Teerikorpi (1990) notes on such biases: ‘a large part, maybe all, of the discrepancy between stellar reddenings and other high-latitude extinction indicators can be ascribed to the reddening bias’. Two kinds of such biases are analysed by **Teerikorpi (1990)**. (i) Due to the Malmquist effect, distant stars in a magnitude limited sample have a bluer average intrinsic colour than such colour of similar stars in a local distance limited sample. (ii) Distant, highly reddened stars tend to remain below the detection limit of a magnitude limited sample. This leads to an underrepresentation of highly reddened stars in such a sample. Hence, its distant stars have a bluer average reddened colour. In turn, such blueward biases of a colour of distant stars lead to an underestimation of the reddening as the difference between the colour of nearby (unreddened) and distant (reddened) stars.

After an analysis of these biases, **Teerikorpi (1990)** suggests that ‘the average reddening reaches $E(B - V) = 0.04$ mag at 400 pc above the Galactic plane’ (**SFD98**).

Both biases are common in reddening maps and models. For example, a previous (albeit rather similar) version of **LVV19** provided by **Lallement et al. (2014, hereafter LVV14)** admits the bias (ii) in their results: ‘There is a limitation in the brightness of the target stars, and the subsequent lack of strongly reddened stars results. . . There is for the same reasons a bias towards low opacities. . .’.

Gontcharov & Mosenkov (2019) discuss another bias – (iii) an overestimation of the intrinsic colours due to the difficulties in the selection of unreddened stars. In other words, this bias originates from a use of slightly reddened stars as unreddened.

¹⁵ All mentioned extinction laws provide similar estimates in the optical range.

¹⁶ **AGG92** apply the constraint $A_{\text{V}} < 0.1$ mag for $|b| \geq 60^\circ$.

¹⁷ This normalization is the reddening-to-emission calibration, which we discuss later in this Section.

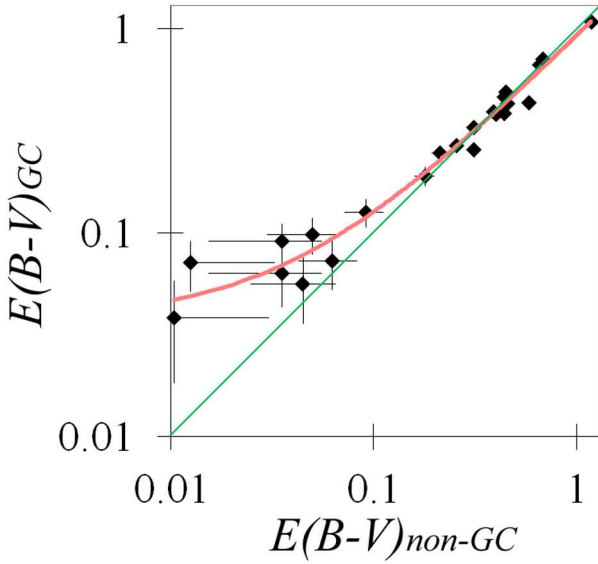


Figure 11. $E(B - V)$ from GSF19 in the non-GC versus GC voxels for the 23 GCs. The linear trend is shown by the thick red line, while the one-to-one relation – by the thin green line.

Note that these biases also may lead to the above mentioned reddening-to-emission calibration systematic errors in SFD98 and MF15 due to underestimation of reddening of stars, quasars and galaxies used in the calibration.

These biases have been eliminated to some extent in the three consecutive versions of the GSF map: Green et al. (2015, hereafter GSF15), Green et al. (2018, hereafter GSF18), and GSF19. GSF18 have recognized the underestimation of low reddenings due to an offset in the colour zero-point of the stellar templates. Therefore, in this sequence of the map versions the new templates are bluer than the old ones. Also, GSF18 has realized that GSF15 ‘tends to infer zero reddening when the true reddening is below a few hundredths of a magnitude.’ As a result, GSF19 provides higher reddenings at high-latitudes than those from GSF15.

5.1 Reddening of Galactic globular clusters

Direct measurements of the extinction and reddening of objects far from the Galactic mid-plane may be an ultimate solution of this issue. However, such measurements are rare. Examples are given by Gontcharov, Mosenkov & Khovritchev (2019); Gontcharov, Khovritchev & Mosenkov (2020) for stars of the Galactic globular clusters (GCs) NGC 5904 (M5) and NGC6205 (M13) at the latitudes of about $+47^\circ$ and $+41^\circ$, respectively. For both the clusters, the optical extinction is found to be twice as high as generally accepted. Thus, high-latitude GCs seem to be promising probes of the reddening across the whole dust layer.

GSF19 is based on *Gaia* DR2 parallaxes and a deep multiband photometry from 2MASS and the Panoramic Survey Telescope and Rapid Response System Data Release 1 (Pan-STARRS DR1, Chambers et al. 2016). This makes GSF19 the first 3D reddening map with accurate reddening estimates far beyond the dust layer at high-latitudes.

GSF19 use thousands GC stars in a typical voxel (space cell) within a GC field to derive their reddening, distance modulus, absolute magnitude, and metallicity. These results agree with those for the same GCs obtained by

Bernard et al. (2014) and Gontcharov, Mosenkov & Khovritchev (2019); Gontcharov, Khovritchev & Mosenkov (2020) from the Pan-STARRS photometry of the same GC stars by another method. The most important that the GSF19’s rather high reddening estimates for these GCs agree with the estimates by Gontcharov, Mosenkov & Khovritchev (2019); Gontcharov, Khovritchev & Mosenkov (2020).

In contrast to the voxels within the GC fields with thousands stars, GSF19 use only a hundred stars in a typical voxel outside the GC fields, far from the Galactic mid-plane. Therefore, the GSF19’s reddening estimates in the GC voxels seem to be more reliable than those in the surrounding non-GC voxels.

We select 23 GCs, whose stars dominate in the corresponding voxels of GSF19. This dominance is evident in colour–magnitude diagrams. Typically, such a diagram contains an order of 10 000 stars for each GC with an accurate photometry. These GCs have a distance < 10.5 kpc from the Sun (taken from the data base of GCs by Harris 1996¹⁸, 2010 revision) and an angular diameter ≥ 10 arcmin (taken from Bica et al. 2019). The latter provides, at least, five adjacent voxels where GC stars dominate.

For each GC, Fig. 11 compares an average GSF19 $E(B - V)$ ¹⁹ estimate in the voxels with a dominance of the GC stars and in surrounding non-GC voxels with virtually no such stars, i.e. those between 2 and 3 radii of the GC. The linear trend

$$E(B - V)_{GC} = 0.038 + 0.893 E(B - V)_{non-GC} \quad (30)$$

with a linear correlation coefficient of 0.99 is shown in Fig. 11 by the thick red curve. The mean GSF19 reddening in all non-GC voxels near the Galactic poles, far from the Galactic mid-plane, is $E(B - V) = 0.015$ mag. Consequently, given equation (30), this provides a GSF19 estimate of the mean reddening across the whole dust half-layer below or above the Sun, derived for the GC stars: $E(B - V) = 0.038 + 0.893 \cdot 0.015 = 0.051$ mag. This value, presented in Table 6, supports our estimates.

The difference between GC and non-GC voxels, shown in Fig. 11 by the thick red curve, is not due to a dust inside the GCs, since this would suggest the presence of such dust only inside the high-latitude GCs. This difference may suggest an underestimation of the reddening across the whole dust half-layer by the conventional approaches. This needs further investigation.

6 CONCLUSIONS

Gaia DR2 provides first accurate parallaxes and optical photometry for a sample of giants in the clump domain of the HR diagram, which is complete for a space across the whole Galactic dust layer near the Sun. In this paper we have used the observables $G_{BP} - G_{RP}$, $G_{RP} - W3$, $M_{G_{BP}} + A_{G_{BP}} = G_{BP} + 5 + 5 \log_{10} \varpi$, $M_{G_{RP}} + A_{G_{RP}} = G_{RP} + 5 + 5 \log_{10} \varpi$, and $M_{W3} + A_{W3} = W3 + 5 + 5 \log_{10} \varpi$. They are based on the *Gaia* DR2 parallaxes ϖ , photometry in the G_{BP} , G_{RP} bands and *WISE* photometry in the $W3$ band. We created a complete sample of 101 810 giants in a space cylinder with the radius 700 pc around the Sun, up to $|Z| < 1800$ pc along the Z Galactic coordinate.

We assumed that the spatial variations of the modes of the observables reflect the spatial variations of the extinction and reddening, in combination with some linear vertical gradients of the intrinsic colours and absolute magnitudes of the giant clump.

¹⁸ <https://www.physics.mcmaster.ca/~harris/mwgc.dat>

¹⁹ Based on the GSF19 extinction law, we adopt $E(B - V) = 1.04E(g_{P1} - r_{P1})$, where g_{P1} and r_{P1} are the Pan-STARRS filters.

This approach allowed us to derive these characteristics of the clump in combination with the estimates of the extinction and reddening along the Galactic mid-plane and across the whole dust layer. We derived the intrinsic colours and absolute magnitudes of the nearby clump giants in a thin coordinate layer and in a narrow vertical cylinder. These two sets of the derived characteristics agree within 0.005 mag. Also, we estimated the vertical gradients of the intrinsic colours and absolute magnitudes of the clump within $|Z| < 1700$ pc by use of the observables in the space beyond the dust layer and the reddening estimates from the **MF15** map.

Finally, for $|Z| < 1.7$ kpc we found:

$$\begin{aligned} M_{\text{GBP}} &= (0.91 \pm 0.01) + (0.01 \pm 0.01) |Z|, \\ M_{\text{GRP}} &= (-0.235 \pm 0.01) + (0.04 \pm 0.01) |Z|, \\ M_{\text{W3}} &= (-1.67 \pm 0.01) + (0.07 \pm 0.01) |Z|, \\ (G_{\text{BP}} - G_{\text{RP}})_0 &= (1.145 \pm 0.01) - (0.03 \pm 0.01) |Z| \text{ and} \\ (G_{\text{RP}} - W3)_0 &= (1.435 \pm 0.01) - (0.03 \pm 0.01) |Z|, \end{aligned}$$

where Z is expressed in kpc. The obtained M_{W3} agrees with the recent literature estimates. The other obtained values have no robust empirical estimates in the literature, since they are obtained for the first time at a precision level of 0.01 mag.

We compared the derived clump intrinsic colours and absolute magnitudes with the theoretical predictions from PARSEC, MIST and IAC-BaSTI. This allowed us to estimate the clump's median age and $[\text{Fe}/\text{H}]$ with their linear vertical gradients within $|Z| < 1.7$ kpc as $(2.3 \pm 0.5) + (3.2 \pm 1.6) |Z|$ Gyr and $(-0.08 \pm 0.08) - (0.16 \pm 0.07) |Z|$, respectively, where Z is expressed in kpc. These results agree with the recent empirical and theoretical estimates, particularly, with those from the review of [Girardi \(2016\)](#). The predictions from the three models agree for the optical bands. However, the PARSEC and MIST predictions disagree for $W3$ (IAC-BaSTI provides no information for $W3$). This may indicate an issue in the MIST colour- T_{eff} relation and/or bolometric correction for $W3$.

Serendipitously, all the models give similar age-metallicity relations by use of our results in the optical range. This similarity suggests that the models converge to a realistic representation of nature. For the ' $(G_{\text{BP}} - G_{\text{RP}})_0$ versus M_{GRP} ' estimates the logarithmic approximation $[\text{Fe}/\text{H}] = 4.56 - 0.495 \log \text{age}$ is the most reliable.

The obtained estimates of the extinction and reddening across the whole dust half-layer below or above the Sun converge to the mean reddening $E(B-V) = 0.06$ mag. This agrees with the recent estimates from the 3D reddening map of **GSF19** for high-latitude Galactic globular clusters, the **G17** map, the **G12** model, and some other studies. Therefore, our estimate favours higher reddenings across the whole dust half-layer w.r.t. the values advocated by **SFD98**, **MF15**, **DCL03**, and **LVV19**. A further investigation of this issue is important for a correct estimation of the extinction for high-latitude extragalactic objects.

DATA AVAILABILITY

The data underlying this article will be shared on reasonable request to the corresponding author.

ACKNOWLEDGEMENTS

We thank the anonymous reviewers and Xiaodian Chen for useful comments, Aaron Dotter, Santi Cassisi and Leonid Petrov for discussion of our results, and Jeremy Mutter for assistance with English syntax.

The research described in this paper makes use of Filtergraph

([Burger et al. 2013](#)), an online data visualization tool developed at Vanderbilt University through the Vanderbilt Initiative in Data-intensive Astrophysics (VIDA) and the Frist Center for Autism and Innovation (FCAI, <https://filtergraph.com>). The resources of the Centre de Données astronomiques de Strasbourg, Strasbourg, France (<http://cds.u-strasbg.fr>), including the SIMBAD database and the X-Match service, were widely used in this study. This work has made use of data from the European Space Agency (ESA) mission *Gaia* (<https://www.cosmos.esa.int/gaia>), processed by the *Gaia* Data Processing and Analysis Consortium (DPAC, <https://www.cosmos.esa.int/web/gaia/dpac/consortium>). This publication makes use of data products from the *Wide-field Infrared Survey Explorer*, which is a joint project of the University of California, Los Angeles, and the Jet Propulsion Laboratory/California Institute of Technology.

REFERENCES

- Arenou F., Grenon M., Gomez A., 1992, *A&A*, 258, 104 (AGG92)
 Bailer-Jones C. A. L., 2015, *PASP*, 127, 994
 Bailer-Jones C. A. L., Rybizki J., Fouvaneau M., Mantelet G., Andrae R., 2018, *AJ*, 156, 58
 Bernard E. J. et al., 2014, *MNRAS*, 442, 2999
 Berry M. et al., 2012, *ApJ*, 757, 166
 Bica E., Pavani D. B., Bonatto C. J., Lima E. F., 2019, *AJ*, 157, 12
 Bovy J., Rix H.-W., Green G. M., Schlafly E. F., D.P. Finkbeiner, 2016, *ApJ*, 818, 130
 Burger D., Stassun K. G., Pepper J., Siverd R. J., Paegert M., De Lee N. M., Robinson W. H., 2013, *Astron. Comput.*, 2, 40
 Cardelli J. A., Clayton G. C., Mathis J. S., 1989, *ApJ*, 345, 245 (CCM89)
 Casagrande L. et al., 2016, *MNRAS*, 455, 987
 Chen Y. Q., Casagrande L., Zhao G., Bovy J., Silva Aguirre V., Zhao J. K., Jia Y. P., 2017, *ApJ*, 840, 77
 Chambers K. C. et al., 2016, arXiv e-prints, arXiv:1612.05560
 Choi J., Dotter A., Conroy C., Cantiello M., Paxton B., Johnson B. D., 2016, *ApJ*, 823, 102
 Davenport J. R. A. et al., 2014, *MNRAS*, 440, 3430 (DIB14)
 Dotter A., 2016, *ApJS*, 222, 8
 Drimmel R., Spergel D. N., 2001, *ApJ*, 556, 181
 Drimmel R., Cabrera-Lavers A., López-Corredoira M., 2003, *A&A*, 409, 205 (DCL03)
 Gaia Collaboration et al., 2018a, *A&A*, 616, A1
 Gaia Collaboration et al., 2018b, *A&A*, 616, A4
 Girardi L., Groenewegen M.A.T., Hatziminaoglou E., da Costa L., 2005, *A&A*, 436, 895
 Girardi, 2016, *ARA&A*, 54, 95
 Gontcharov G. A., 2008, *Astron. Lett.*, 34, 785
 Gontcharov G. A., 2009, *Astron. Lett.*, 35, 638
 Gontcharov G. A., 2012a, *Astron. Lett.*, 38, 12
 Gontcharov G. A., 2012b, *Astron. Lett.*, 38, 87 (G12)
 Gontcharov G. A., 2012c, *Astron. Lett.*, 38, 694
 Gontcharov G. A., 2013, *Astron. Lett.*, 39, 550
 Gontcharov G. A., 2016a, *Astron. Lett.*, 42, 445
 Gontcharov G. A., 2016b, *Astrophysics*, 59, 548
 Gontcharov G. A., 2017a, *Astron. Lett.*, 43, 472 (G17)
 Gontcharov G. A., 2017b, *Astron. Lett.*, 43, 545
 Gontcharov G. A., Mosenkov A. V., 2018, *MNRAS*, 475, 1121
 Gontcharov G. A., 2019, *Astron. Lett.*, 45, 605
 Gontcharov G. A., Mosenkov A. V., 2019, *MNRAS*, 483, 299
 Gontcharov G. A., Mosenkov A. V., Khovritchev M. Yu., 2019, *MNRAS*, 483, 4949
 Gontcharov G. A., Khovritchev M. Yu., Mosenkov A. V., 2020, *MNRAS*, 497, 3674
 Green G. M. et al., 2015, *ApJ*, 810, 25 (GSF15)

- Green G. M. et al., 2018, MNRAS, 478, 651 (GSF18)
- Green G. M., Schlafly E., Zucker C., Speagle J. S., Finkbeiner D., 2019, ApJ, 887, 93 (GSF19)
- Harris W. E., 1996, AJ, 112, 1487
- Hawkins K., Leistedt B., Bovy J., Hogg D. W., 2017, MNRAS, 471, 722
- Hidalgo S. L. et al., 2018, ApJ, 856, 125
- Huang Y. et al., 2015, Res. Astron. Astrophys., 15, 1240
- Jurić M. et al., 2008, ApJ, 673, 864
- Lallement R., Vergely J. L., Valette B., Puspitarini L., Eyer L., Casagrande L., 2014, A&A, 561, A91 (LVV14)
- Lallement R., Babusiaux C., Vergely J. L., Katz D., Arenou F., Valette B., Hottier C., Capitanio L., 2019, A&A, 625, A135 (LVV19)
- Marigo P. et al., 2017, ApJ, 835, 77
- Meisner A. M., Finkbeiner D. P., 2015, ApJ, 798, 88 (MF15)
- Michalik D., Lindegren L., Hobbs D., 2015, A&A, 574, A115
- Önal Taş Ö., Bilir S., Seabroke G. M., Karaali S., Ak S., Ak T., Bostanci Z. F., 2016, Publications of the Astronomical Society of Australia, 33, 44
- Parenago P. P., 1954, A Course in Stellar Astronomy [in Russian]. GITTL, Moscow
- Paxton B., Bildsten L., Dotter A., Herwig F., Lesaffre P., Timmes F., 2011, ApJS, 192, 3
- Paxton B. et al., 2013, ApJS, 208, 4
- Perryman M., 2009, Astronomical Applications of Astrometry: Ten Years of Exploitation of the Hipparcos Satellite Data. Cambridge Univ. Press, Cambridge, UK
- Reimers D., 1975, Memoires of the Societe Royale des Sciences de Liege, 8, 369
- Robin A. C., Reylé C., Derrière S., Picaud S., 2003, A&A, 409, 523
- Ruiz-Dern L., Babusiaux C., Arenou F., Turon C., Lallement R., 2018, A&A, 609, A116 (RBA18)
- Schlegel D. J., Finkbeiner D. P., Davis M., 1998, ApJ, 500, 525 (SFD98)
- Skrutskie M.F. et al., 2006, AJ, 131, 1163
- Schlafly E. F. et al., 2016, ApJ, 821, 78 (SMS16)
- Soubiran C., Bienaymé O., Mishenina T. V., Kovtyukh V. V., 2008, A&A, 480, 91
- Teerikorpi P., 1990, A&A, 235, 362
- van Leeuwen F., 2007, A&A, 474, 653
- Vergely J.-L., Freire Ferrero R., Egret D., Köppen J., 1998, A&A, 340, 543
- Wang S., Chen X., 2019, ApJ, 877, 116 (WC19)
- Wright E. L. et al., 2010, AJ, 140, 1868
- Yaz Gökçe E., Bilir S., Öztürkmen N. D., Duran Ş., Ak T., Ak S., Karaali S., 2013, New Astron., 25, 19

This paper has been typeset from a $\text{\TeX}/\text{\LaTeX}$ file prepared by the author.